Surfaces and Interfaces 61 (2025) 106143

Contents lists available at ScienceDirect

Surfaces and Interfaces

journal homepage: www.sciencedirect.com/journal/surfaces-and-interfaces

Microwave-assisted synthesis of hierarchical BiOBr/BiOF Z-scheme heterojunction with abundant oxygen vacancies for activating peroxymonosulfate toward photodegradation of the refractory levofloxacin

Guohua Dong [a,*], Dongzhe Zhang [a], Xinjia Zhang [b,*], Zhuangfang Zhang [a], Dong-feng Chai [a], Lijian Meng [d], Wanxia Tang [a], Ming Zhao [a,c], Wenzhi Zhang [a,*]

[a] College of Chemistry and Chemical Engineering, Qiqihar University, Qiqihar 161006, PR China
[b] College of Light Industry and Textile, Qiqihar University, Qiqihar 161006, PR China
[c] Innovation Center of Industrial Hemp for State Market Regulation, Qiqihar University, Qiqihar 161006, PR China
[d] CIEIT/ISEP, Instituto Politecnico do Porto, 4249-015 Porto, Portugal

ARTICLE INFO

Keywords:
BiOBr/BiOF heterojunction
Z-scheme
Peroxymonosulfate
Levofloxacin
Photodegradation

ABSTRACT

Herein, a novel Z-scheme BiOBr/BiOF heterojunction was synthesized via one-step microwave-assisted hydrothermal method, which was integrated with peroxymonosulfate (PMS) to design a sulfate radical ($\bullet SO_4^-$) based advanced oxidation processes (AOPs) system through PMS activation (BiOBr/BiOF-PMS) toward Levofloxacin (LFX) photodegradation. In order to achieving an optimal degradation efficiency, the formed BiOBr/BiOF-PMS was systematically investigated and the operational parameters for LFX photodegradation were thoroughly optimized. Thereby, the optimal BiOBr/BiOF exhibits a higher photodegradation efficiency of 89.8 % toward LFX via PMS activation compared to others including PMS alone, BiOBr, BiOF and BiOBr/BiOF with varied ratios. Furthermore, the BiOBr/BiOF has superior stability for multiple cycles and universal applicability for degrading various contaminants. This can mainly be attributed that the formed heterojunction between BiOBr and BiOF and the enhanced concentration of oxygen vacancies (OVs) of BiOBr/BiOF heterojunction, which can synchronously promote the separation and transmission of the photogenerated charges (e^-/h^+) and thereby lead to more reactive oxygen species (ROS). As well, the expanded optical responsiveness and increased specific surface area of BiOBr/BiOF are also mainly responsible for the improved photodegradation capability. Free radical capture experiments and ESR technique verify that the $\bullet O_2^-$ is the primary ROS and $\bullet SO_4^-$ and $\bullet OH$ play subordinative role. The photodegradation pathways of LFX were unraveled based on the identified intermediates with a liquid-chromatography-mass (LC-MS) technique. Consequently, this study offers a novel route by developing Bi-based heterojunction photocatalyst to activate PMS for refractory antibiotic photodegradation.

1. Introduction

Large amounts of antibiotics discharged into the natural water body have brought about severe environmental contamination and eco-catastrophe, which has garnered considerable attention on account of their potential toxicity and uncontrollable threats to the environment and human beings [1,2]. Among them, LFX, as one of typical third-generation broad-spectrum quinolone antibiotics, has been widely utilized in clinical practice to treat diseases and prevent infections. However, its excessive use and scale-up production have also brought serious environmental pollution problems, which have aroused considerable attention due to its potential toxicity and difficulty to metabolize by humans and animals. It is reported that the average concentration of LFX in sewage treatment plants can reach an astounding level approximately 2000 $ng{\cdot}L^{-1}$ [3]. Therefore, addressing the problem relative to antibiotic contamination has emerged as a crucial concern in contemporary society [4,5]. Over the last several years, various traditional wastewater treatment techniques including adsorption, biological treatment, electrocoagulation, flocculation, ion exchange, membrane separation and reverse osmosis have been extensively employed to convert antibiotics into less harmful or non-toxic states in order to reduce pollution risk [6,7]. However, these methods

* Corresponding authors.
E-mail addresses: ghdong@qqhru.edu.cn (G. Dong), xjzhang@qqhru.edu.cn (X. Zhang), zhangwenzhi@qqhru.edu.cn (W. Zhang).

https://doi.org/10.1016/j.surfin.2025.106143
Received 28 November 2024; Received in revised form 27 February 2025; Accepted 28 February 2025
Available online 1 March 2025

commonly suffer from severe drawbacks, such as excessive sludge formation, extreme energy consumption, low removal efficiency, high cost and the generation of secondary pollutants [8]. Accordingly, it is quite imperative to explore a reliable and efficient degradation method to accomplish the complete removal of toxic antibiotics.

Semiconductor photocatalysis, as a fascinating AOPs technology, has been intensively investigated in the degradation of various refractory organic pollutants due to it is numerous advantages such as easy to operation, low cost, low energy consumption and environmental compatibility [9,10]. Especially, photocatalysis coupled with PMS activation shows greater potential to degrade organic pollutants thanks to the formation of $\bullet SO_4^-$ with higher redox potential (2.5–3.1 V vs. NHE), longer half-life (30–40 μs vs. 20 ns) and a wider pH operating range (2∼8) compared to hydroxyl radical (•OH) [11]. In this context, the exploration of photocatalysts with high efficiency and low-cost is still extremely important to improve the degradation efficiency and promote the practical applicability of photocatalysis [12].

In recent decades, as typical anisotropic two-dimensional (2D) semiconductor material with an appropriate bandgap (2.4–2.9 eV), BiOBr has attracted widespread attention in the photocatalytic field due to low cost, non-toxicity, chemical stability and large specific surface area, etc. Especially, owing to its unique layered structure consisting of positive $[Bi_2O_2]^{2+}$ layers and negative halogen ion plates, there is a strong internal electrostatic field in its own crystal structure, which can effectively facilitate the separation and transportation of the e^-/h^+ [13]. However, as an indirect bandgap semiconductor, its photocatalytic degradation process still suffer from some limitations because of the rapid recombination of photogenerated e^-/h^+ [14]. Recently, numerous efforts have been concentrated on the modification of BiOBr for improving its photocatalytic performance, e.g., elemental doping, defect engineering, morphology modulation and heterojunction construction (Type-II heterojunction, S-scheme and Z-scheme, etc.). Generally, constructing a heterojunction is a widely used strategy for improving the photocatalytic performance of monomer photocatalyst, which can effectively accelerate the separation and transfer together with simultaneously inhibit the recombination of the e^-/h^+ [15–17]. In particular, Z-scheme heterojunction photocatalysts have attracted widespread attention due to their ability to retain strong redox capabilities of each monomer [18–20]. In addition, it is reported that the inducing OVs on the surface and inside the photocatalyst can be an efficacious strategy to improve the performance of the photocatalyst, which can enable to modulate the electronic structure, extend light response, regulate band gap, alter the positions of conduction and valence bands (CB and VB) of the photocatalyst, finally leading to the significant improved photocatalytic performance.

Herein, a novel Z-scheme BiOBr/BiOF heterojunction photocatalysts with abundant OVs was synthesized via a facile one-step microwave-assisted hydrothermal method and thereby utilized to construct a $\bullet SO_4^-$ radical based AOPs system (BiOBr/BiOF-PMS) by integrating with PMS for degrading the refractory LFX contaminants. The BiOBr/BiOF was subjected to a detailed characterization with a series of combined techniques including SEM, TEM, FT-IR, XRD, XPS, etc. The photodegradation properties of BiOBr/BiOF-PMS were optimized and evaluated by investigating the LFX removal efficiencies under various catalyst dosages, pH values, the initial concentration of antibiotic and PMS. Furthermore, free radical capture assays and ESR testing were utilized to investigate the ROS and unravel the possible photodegradation mechanism. The possible photodegradation pathway of LFX was investigated by checking the intermediates using LC-MS technique. To sum up, this work offers a novel route for improving the photocatalytic performance of bismuth oxyhalide by synchronously integrating construction of heterojunction and induction of OVs for contaminants removal via PMS activation.

2. Materials and methods

2.1. Materials and chemicals

All reagents were analytical grade and used directly without further purification. The deionized water was employed throughout the experiment. Detailed information about the chemicals and reagents is provided in the **supporting information (Text S1).**

2.2. Preparation of BiOBr/BiOF

The BiOBr/BiOF was prepared with a microwave-assisted hydrothermal method. Typically, 1 mmol $Bi(NO_3)_3{\cdot}5H_2O$ were thoroughly dissolved into 30 mL ethylene glycol (EG) and then 1 mmol mixture of KBr and NH_4F with different molar ratio of Br and F was introduced into the above solution under continuously stirring for 1 h. Subsequently, the obtained solution was transferred into a 100 mL PTFE microwave reactor and the reactor was sealed and suffered from heating treatment at 160 °C for 1 h in a microwave reaction apparatus with power of 5000 W at frequency of 2450 MHz. After naturally cooling to room temperature, the powders product was collected by a series of sequential treatments including centrifugation and cleaning with deionized water and ethanol for several times. The resulting BiOBr/BiOF was obtained by drying the powders in an oven at 70°C for 8 h. In order to obtain the optimal catalysts, the molar ratios of KBr to NH_4F were selected as 4:1, 2:1, 1:1 and 1:2 and the obtained photocatalysts were designated as BiOBr-4/BiOF-1, BiOBr-2/BiOF-1, BiOBr-1/BiOF-1 (BiOBr/BiOF) and BiOBr-1/BiOF-2, respectively. It needs to be noted that the above formed products were uniformly simplified as BiOBr/BiOF in the following explanation without special emphasis.

Additionally, the pure BiOBr and BiOF were also synthesized with merely adding KBr (1.0 mmol) or NH_4F (1.0 mmol) besides $Bi(NO_3)_3{\cdot}5H_2O$ (1.0 mmol) using the identical method, which were utilized to contrast with the BiOBr/BiOF compounds.

2.3. Material characterization

The specific information of material characterization is explained in the **supporting information (Text S2).**

2.4. Photocatalytic degradation experiment

The photodegradation experiment was performed in a quartz glass photoreactor equipped with magnetic agitator and condensing apparatus system with circulating water (BL-GHX-V, China), which can ensure the photoreaction in a constant room temperature ∼25°C. A 500 W xenon lamp was selected as the light source for persistent supply of energy and the used light intensity was modulated to 100 $mW{\cdot}cm^{-2}$ for simulating the solar light. The internal schematic diagram of the photocatalytic instrument is shown in **Fig. S1**. Typically, under magnetic stirring, a certain amount of catalyst is uniformly dispersed into 50 mL of LFX solution with a specified concentration. Subsequently, the above reactive solutions were maintained in dark conditions for 30 min to achieve adsorption-desorption equilibrium. After that, the photocatalytic degradation was carried out by adding PMS in a specific proportion and then turning on the xenon lamp light source. 5 mL aliquots were subsequently taken out at 30 min intervals and treated by centrifugation approach to remove the residue photocatalyst. Then, the clarified supernatant liquid was collected and measured using a UV–visible spectrophotometer (TU-1900, China) at the maximum absorption wavelength of LFX ($\lambda = 289$ nm) to analyze the concentration of residual LFX. Finally, the photocatalytic degradation efficiency of LFX was evaluated according to Eq. (1):

$$\textit{Degradation efficiency}\ (\%) = [(C_0 - C_t)/C_0] \times 100 = [(A_0 - A_t)/A_0] \quad (1)$$

where C_0 and C_t are the concentration of LFX at time 0 and t, while A_0 and A_t refer to the absorbance intensities of the LFX solution at time 0 and t, respectively [21].

Furthermore, the photodegradation process of LFX was investigated utilizing the pseudo first-order reaction kinetic model as the following formula (2):

$$\ln C_t/C_0 = -k_{app}t \quad (2)$$

where k_{app} stands for the apparent rate constant (min^{-1}). C_0 and C_t resemble the formula (1).

It is noted that the relative photocatalytic operation parameters were detailly optimized by varying the concentration of PMS (0.5 $mmol{\cdot}L^{-1}$, 1 $mmol{\cdot}L^{-1}$, 1.5 $mmol{\cdot}L^{-1}$, 2 $mmol{\cdot}L^{-1}$), initial concentration of LFX (5 $mg^{-1}{\cdot}L^{-1}$, 10 $mg^{-1}{\cdot}L^{-1}$, 20 $mg^{-1}{\cdot}L^{-1}$, 30 $mg^{-1}{\cdot}L^{-1}$ and 40 $mg^{-1}{\cdot}L^{-1}$), applied dosage of the catalysts (5 mg, 10 mg, 20 mg, 30 mg and 40 mg) and solution pH values (3, 5, 7, 9 and 11), respectively. In addition, the degradation intermediates of LFX were identified by the LC-MS technique. The stability and reusability of the catalysts were investigated by multiple recycle degradation experiments under identical conditions. The as-used catalysts were collected with centrifugation approach and washed with deionized water for removing the residual substance. Furthermore, the FT-IR, XPS and SEM of the catalyst before and after utilization were compared to assess the variation of composition, crystalline structure and morphology of the catalyst. To analyze the mineralization degree of LFX by BiOBr/BiOF in the photocatalysis, total organic carbon (*TOC*) removal efficiency was calculated according to expression (3):

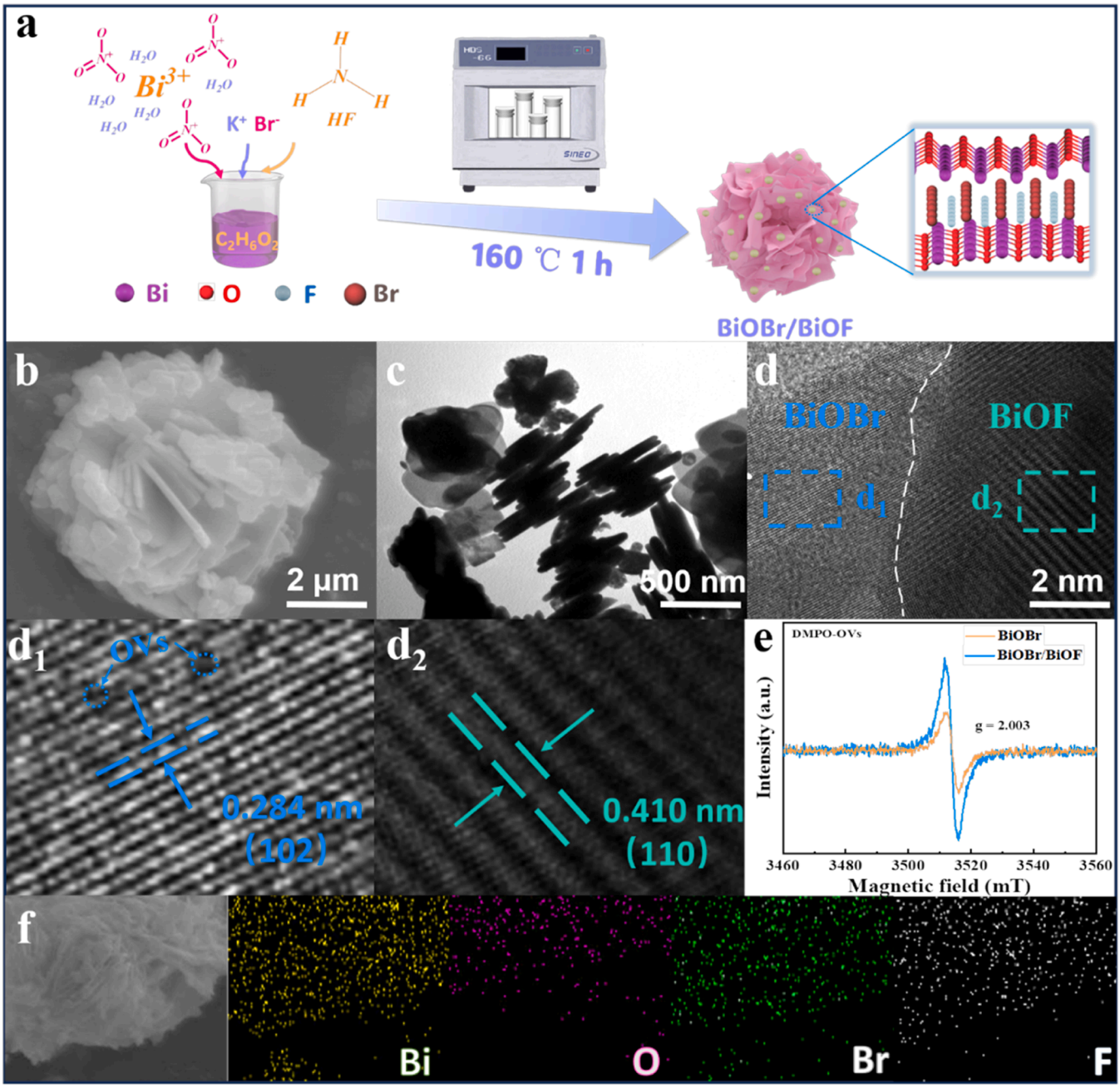

Fig. 1. (a) Schematic illustration of the fabrication process of BiOBr/BiOF (b) the Scanning electron microscopy (SEM image), (c) Transmission electron microscopy (TEM) image and (d, d_1 and d_2) high-resolution-TEM (HR-TEM) images of BiOBr/BiOF (e) the electron spin resonance (ESR) spectra of BiOBr and BiOBr/BiOF (f) the energy dispersive spectrometer (EDS) elemental mapping images of BiOBr/BiOF.

$$TOC\ removal\ efficiency = [(TOC_0 - TOC) / TOC_0] \times 100\ \% \quad (3)$$

where, TOC_0 and TOC are the TOC values of the LFX solution and in the degradation solution sample, respectively [22].

All photodegradation experiments were conducted in triplicate and the gained results were statistically calculated using the analysis of variance (ANOVA) method, which are displayed as the average of the measurements with error bars representing the relative deviation from this average. The variables were analyzed based on their impact on the response at a 95 % confidence level, with a significance threshold of $p < 0.05$.

2.5. Photoelectrochemical measurement

The detailed description of photoelectrochemical measurements is shown in the **supporting information (Text S3).**

2.6. Antibacterial activity

The toxicity of the degraded LFX solution was evaluated by performing the antibacterial activity experiments with Escherichia staphylococcus aureus bacteria as representative strains. Specifically, a meat peptone culture medium (MPCM) was prepared by dissolving 25.0 g NaCl, 12.5 g yeast extract, 10.0 g tryptone and 15.0 g agar powder into 1000 mL deionized water in a clean beaker under heating for a certain time. The above MPCM (10 mL) was transferred into a petri dish with diameter of 10 cm and then sterilized at 120 °C for 20 min. Then, 200 μL bacterial solution was added the MPCM in petri dish. The dried filter papers with existence of different LFX solutions including the original and degraded solution were evenly distributed on the surface of the above MPCM. After incubating for 24 h at 37 °C, the antibacterial activity was evaluated by measuring the diameter of the clear inhibitory zones in millimeter.

3. Results and discussion

As schematically illustrated in Fig. 1a, the flower-like BiOBr/BiOF was synthesized by facile one-step microwave-assisted hydrothermal method using $Bi(NO_3)_3{\cdot}5H_2O$, KBr and NH_4F as feedstocks. The morphology and microstructure of the synthesized samples were characterized by performing the SEM and TEM measurements. From the SEM image in Fig. 1b, it can be easily seen that the BiOBr/BiOF has a flower-like morphology composed of irregular nanosheets with almost similar thickness. In contrast, both of the synthesized BiOBr and BiOF display microsphere-like morphology with significant agglomeration (**Fig. S2)**. Thereby, it can be reasonably speculated that the regulation on the ratio of F^- and Br^- can effectively control the crystallization and growth process of the resultant product, finally leading to various morphology of the resultant catalyst. In view of the above confirmation, we can assertively infer that the BiOBr/BiOF has larger specific surface area and higher pore distribution than those of BiOBr and BiOF, which is commonly conducive to the photocatalytic activity due to the existence of abundant reactive sites on the surface of samples [23].

From the TEM image in Fig. 1c, we can observe that the BiOBr/BiOF exhibits a distinct lamellar structure with an almost similar thickness that was stacked with each other. By comparison, the discrepancy of the morphology of BiOBr/BiOF in SEM and TEM can mainly be due to the destruction of the layered flower-like morphology of BiOBr/BiOF under ultrasonic effect for preparing TEM sample. Furthermore, the HR-TEM images of BiOBr/BiOF in Fig. 1d exhibit distinct lattice fringes with interplanar spacings of 0.284 nm and 0.410 nm, which correspond to the (102) crystal planes of BiOBr (Fig. 1d_1) and the (110) crystal planes of BiOF (Fig. 1d_2), respectively [24,25]. This directly proves the successful construction of the heterojunction between BiOBr and BiOF. Additionally, the discontinuity on lattice stripes in BiOBr/BiOF may be related to the presence of oxygen vacancies (OVs) [26]. This can mainly be attributed that microwave-assisted hydrothermal method can promote the thermal motion of water molecules at high temperatures and thereby accelerat the desorption of oxygen atoms from the surface or interior of materials, finally leading to the formation of OVs [27]. From the selected area electron diffraction (SAED) pattern in **Fig. S3**, we can clearly see two sets of bright electron diffraction spots marked with blue and green circles, which correspond to the (001), (110) and (102) planes of BiOBr and the (110) plane of BiOF, manifesting the formation of BiOBr/BiOF heterojunction. As shown in Fig. 1e**,** the higher ESR signal of BiOBr/BiOF compared to the pure BiOBr is mainly attributed that the BiOBr/BiOF possesses the higher concentration of OVs, which is conventionally conducive to the improvement of photocatalytic performance [28]. In addition, the EDS analysis in Fig. 1f reveals that the BiOBr/BiOF consists of Bi, O, Br and F elements, further confirming the successful synthesis of binary BiOBr/BiOF heterojunction.

The crystal structure of BiOBr, BiOF and BiOBr/BiOF were demonstrated by XRD measurements. As shown in Fig. 2a, the diffraction peak at 11.6°, 25.3°, 31.7°, 32.2°, 57.3° and 76.5° in the XRD pattern of BiOBr can be assigned to the (001), (101), (102), (110), (212) and (310) crystal planes of BiOBr (JCPDS#01–073–2061) [29]. The diffraction peaks located at 27.7°, 31.7°, 44.2° and 53.7° in the XRD pattern of BiOF can be attributed to the (101), (110), (112) and (211) crystal planes of BiOF (JCPDS#04–010–1921) [30]. The BiOBr/BiOF contains the characteristic diffraction peaks of BiOBr and BiOF, confirming the successful construction of BiOBr/BiOF heterojunction. The surface functional groups of the synthesized samples including BiOBr, BiOF and BiOBr/BiOF were investigated by performing the FT-IR measurements. As depicted in Fig. 2b, it is evident that each sample exhibits well-defined absorption peaks at a wavenumber of 515 cm^{-1}, which can be attributed to the symmetric stretching vibrational mode associated with the Bi-O bond [31]. Additionally, the prominent peak observed at 3480 cm^{-1} is in accordance with the bending vibration of hydroxyl groups (-OH) [32]. As for BiOBr, the peaks in the region of 1050 cm^{-1} and 1390 cm^{-1} are assigned to the Bi-Br band stretching vibration. The absorption peak located at 1620 cm^{-1} corresponds to the symmetric stretching vibration of the Br-Br bond [33]. Furthermore, the absorption peak at 1080 cm^{-1} in BiOF is ascribed to the Bi-F bond [34]. From the FT-IR spectrum of BiOBr/BiOF, we can discern all the characteristic peaks of BiOBr and BiOF, indicating the successful synthesis of BiOBr/BiOF. The decrease in OH concentration demonstrates that hydrogen bonds are the main interactions between BiOBr and BiOF in the BiOBr/BiOF heterojunction.

To further determine the surface elemental composition and chemical state of the BiOBr/BiOF, the XPS characterization was performed. As depicted in Fig. 2c, the XPS survey spectrum of BiOBr/BiOF reveals the presence of Bi, O, Br and F elements. Also, we can see the appearance of unintentional C 1s XPS core level at approximately 284.6 eV in the XPS spectrum, which can be attributed to the unavoidable presence of carbonaceous material within the calibration apparatus. In Fig. 2d, the high-resolution Bi 4f XPS spectra exhibit two peaks at binding energy of 164.2 eV and 158.9 eV, which can be attributed to the Bi $4f_{7/2}$ and Bi $4f_{5/2}$ states, confirming the existence of oxidation state of Bi^{3+} and corresponding to the energy band of Bi-O [35]. The O 1s XPS signal (Fig. 2e) exhibits asymmetry distributions and can be deconvoluted into four peaks located at 533.7 eV, 532.0 eV, 530.3 eV and 529.3 eV, which are related to the hydroxyl, OVs, oxygen atoms in the vicinity of OVs and lattice oxygen in the BiOBr/BiOF [36]. Moreover, it is evident that the binding energy of oxygen atoms in BiOBr/BiOF shows almost no movement, while the peaks of lattice oxygen and vacancy oxygen are moved to a higher binding energy, indicating the changes of chemical atmosphere due to the replacement of Br^- ions by F^- ions in the complex. By further comparison, we can find that the concentration of OVs in the BiOBr/BiOF shows an apparent increase. This may be due to the formation of heterojunctions and the incorporation of surface hydroxyl oxygen into the lattice in the microwave-assisted hydrothermal method. Undoubtedly, the increase of the concentration of OVs can effectively

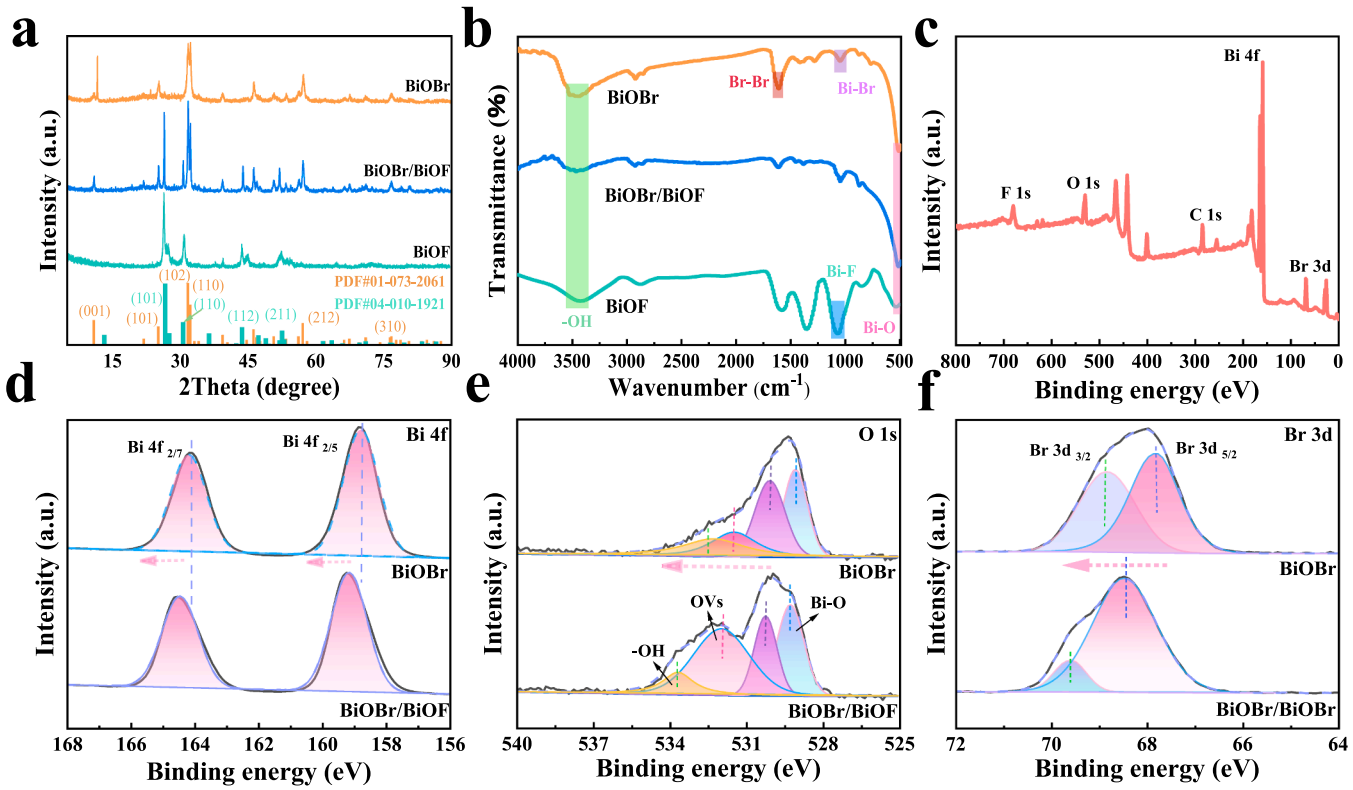

Fig. 2. (a) X-ray powder diffraction (XRD) patterns and (b) Fourier Transform infrared Spectroscopy (FT-IR) spectra of BiOBr, BiOF and BiOBr/BiOF (c) the survey X-ray photoelectron spectroscopy (XPS) spectrum of BiOBr/BiOF and the high-resolution XPS spectra related to BiOBr and BiOBr/BiOF: (d) Bi4f, (e) O1s and (f) Br3d.

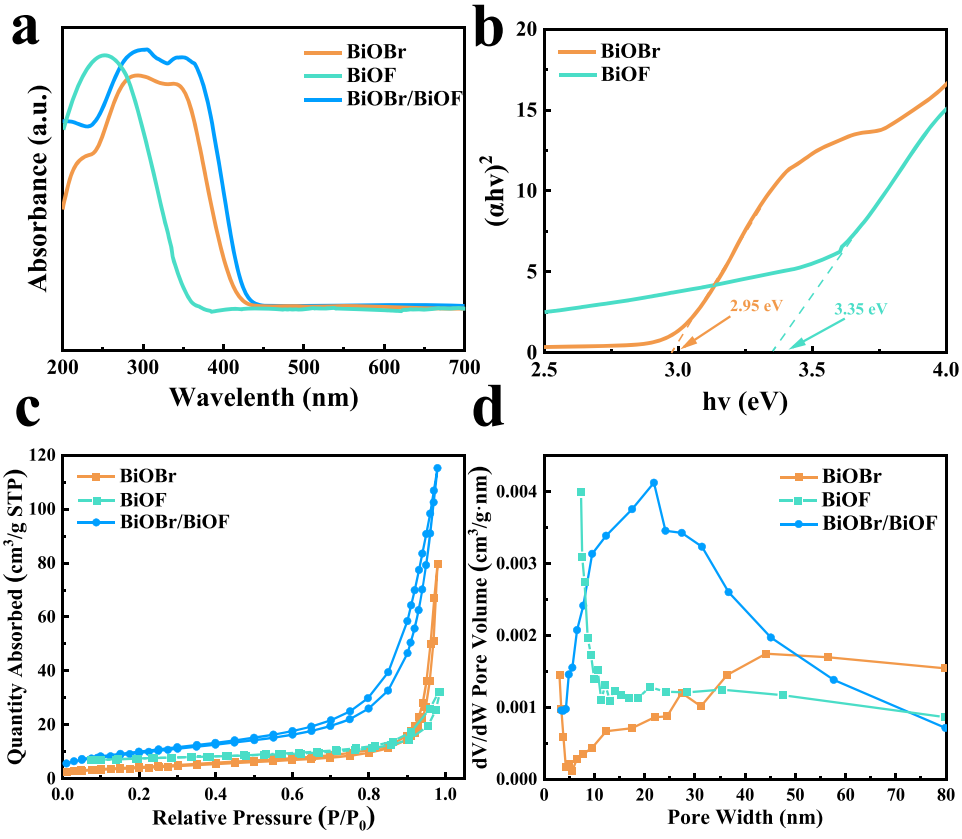

Fig. 3. (a) UV–vis diffusion reflectance spectra (DRS) of BiOBr, BiOF and BiOBr/BiOF (b) the Tauc plots of BiOBr and BiOF (c) N_2 adsorption-desorption isotherm curves and (d) the pore size distribution plots of BiOBr, BiOF and BiOBr/BiOF.

enhance the photocatalytic activity of BiOBr/BiOF by increasing the electron enrichment and promoting the formation of free radicals in photocatalytic reactions. The reduction in hydroxyl concentration is attributed to the migration of oxygen atoms during the process of sample synthesis, which is consistent with the FT-IR results. From Fig. 2f, the high-resolution Br 3d spectra are deconvoluted into two peaks at 68.9 eV and 67.9 eV, which can be attributed to Br $3d_{3/2}$ and Br $3d_{5/2}$, respectively [37]. Compared to bare BiOBr, we can see that the high-resolution Br 3d XPS peaks of BiOBr/BiOF shift to a higher binding energy, implying a decrease in the electron cloud density around Br ions in BiOBr/BiOF. Finally, the high-resolution F 1s XPS spectrum (**Fig. S4**) at binding energy of 682.8 eV confirm that the F^- can be found within the BiOF [38]. Consequently, the changes in elemental binding energy directly reflects the variations of electron density of element and the electron diffusion between different elements finally providing evidence of the successful synthesis of BiOBr/BiOF composite [39].

The UV–vis diffuse reflectance spectroscopy (UV–vis-DRS) was performed to investigate the optical absorption properties of the as-prepared samples. As depicted in Fig. 3a, the optical absorption edges for BiOBr, BiOF and BiOBr/BiOF were observed at approximately 420 nm, 360 nm and 440 nm, respectively. The light absorption range of the BiOBr/BiOF shows a significant redshift compared with the bare monomers, confirming better utilization ability for the visible light. Thereby, the band gap energy of the photocatalysts were calculated using the Kubelka-Munk function ($\alpha h\upsilon = A(h\upsilon - E_g)^{n/2}$), where α denotes the absorption coefficient, Eg reflects the band gap value of semiconductor and A refers to the absorption, hυ stands for the photon energy and n = 1 for direct transition [40]. From the Tauc plots in Fig. 3b, we can observe that the optical gap values are 2.95 eV and 3.35 eV for BiOBr and BiOF, which are consistent with previous reports [41,42]. The N_2 adsorption-desorption isotherms were collected to further examine the textural structure of the prepared photocatalysts. As demonstrated in Fig. 3c, all the obtained catalysts exhibits a typical IV type adsorption-desorption isotherm with an H3 hysteresis ring, indicating the presence of a mesoporous framework within the layered catalysts [43]. The corresponding pore size distribution curves (Fig. 3d) show that the pores in BiOF have sizes ranging from 2 nm to 5 nm, indicating the presence of mesoporous in the material surfaces. The pore size distribution in BiOBr encompasses both mesoporous and microporous range. The existence of mesoporous is associated with the two-dimensional lamellar surface structure of BiOBr, while the presence of micropores is related to the spherical structure of BiOBr. The pore size of BiOBr/BiOF is primarily distributed in the large pore size range, which is attributed to the formation of a flower-like heterojunction between BiOBr and BiOF, resulting in their mutual coverage and reducing the number of mesopores on the surface of BiOBr. The detailed parameters of the specific surface area and pore sizes distribution are presented in **Table S1**. The specific surface areas of BiOBr, BiOF and BiOBr/BiOF are 12.858 $m^2 \cdot g^{-1}$, 5.190 $m^2 \cdot g^{-1}$ and 31.269 $m^2 \cdot g^{-1}$, respectively. The larger specific surface area of BiOBr/BiOF will facilitate the adsorption of target pollutants in water and expose more reactive sites, which provides a structural basis for highly photodegradation performance toward LFX [44].

In view of the superior properties of BiOBr/BiOF than that of BiOBr and BiOF, we systematically evaluated the effects of different catalytic systems (including PMS alone, monomers-PMS and BiOBr/BiOF composites-PMS) on the photodegradation efficiency of LFX. It is noted that all the degradation conditions are consistent besides the types of the prepared catalysts. As shown in Fig. 4a, the degradation efficiency of LFX in the presence of PMS alone exhibits a minor level reaching only 15.6 %. Nevertheless, upon the addition of monomer photocatalysts (BiOBr and BiOF) within the system, there is a slight enhancement for the degradation efficiency of LFX to approximately 44.8 % and 24.0 %, respectively. Excitingly, the significant improvement of the degradation efficiency of LFX can be confirmed by the BiOBr/BiOF composites (BiOBr-4/BiOF-1, BiOBr-2/BiOF-1, BiOBr/BiOF and BiOBr-1/BiOF-2). When the molar ratio of Br and F is 1:1, the formed BiOBr/BiOF delivers the highest degradation efficiency is 80.2 %. From Fig. 4b, we can

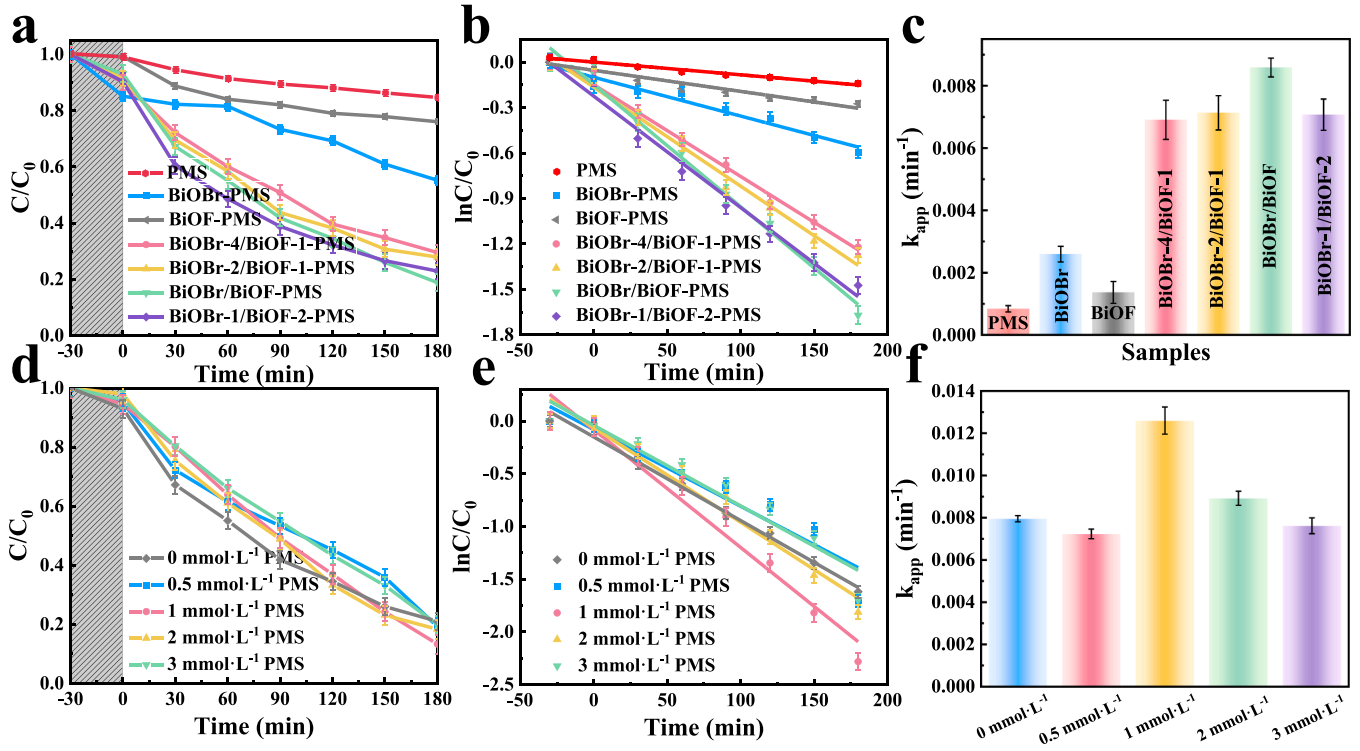

Fig. 4. (a) Comparison of the photocatalytic systems for LFX photodegradation (Conditions: [catalyst] = 10 mg, [LFX] = 10 mg·L^{-1}, pH = 7, [PMS] = 0.5 mmol·L^{-1}), (d) the optimization on the PMS addition amount, (b, e) the profiles of the first-order kinetics derived from Fig. 4(a, d) and (c, f) the corresponding histograms of k_{app} values to Fig. 4(b, e). Error bars indicate the standard deviations derived from three independent experiments.

observe that the degradation of LFX by varied systems satisfy the first-order kinetic process. As shown in Fig. 4c, the obtained k_{app} values are 0.0008 min^{-1} (PMS), 0.0026 min^{-1} (BiOBr-PMS), 0.0014 min^{-1} (BiOF-PMS), 0.0071 min^{-1} (BiOBr-4/BiOF-1-PMS), 0.0071 min^{-1}(BiOBr-2/BiOF-1-PMS), 0.0086 min^{-1} (BiOBr/BiOF-PMS) and 0.0071 min^{-1} (BiOBr-1/BiOF-2-PMS), respectively. The maximum k_{app} value of 0.0086 min^{-1} suggests that the BiOBr/BiOF-PMS is the optimal system toward LFX photodegradation via PMS activation. Hereafter, the following optimizations were performed based on the BiOBr/BiOF-PMS for further improving the photodegradation performance.

Afterward, we further optimized the concentration of PMS addition in the system. As illustrated in Fig. 4d, with the concentration of PMS increasing from 0 mmol·L^{-1} to 3 mmol·L^{-1}, the degradation efficiency of LFX shows a trend of initially increasing and then decreasing and the highest degradation efficiency of LFX of 86.8 % can be obtained at 1 mmol·L^{-1} PMS. Moreover, the degradation process of LFX also comply to the pseudo first-order kinetic model (Fig. 4e) and the biggest k_{app} value is 0.0122 min^{-1} for the 1 mmol·L^{-1} PMS (Fig. 4f). This may be attributed to the insufficient generation of $•SO_4^-$ free radicals at a lower concentration of PMS and conversely the scavenging phenomenon of formed radicals ($•SO_4^-$ and •OH) by the excessive PMS, finally leading to the abundant generation of reactive radicals and low reactivity in the system.

The effect of the initial LFX concentration on LFX photodegradartion in the BiOBr/BiOF-PMS system is depicted in Fig. 5a. As the initial concentration of LFX increases from 5 mg·L^{-1} to 40 mg ·L^{-1}, the removal efficiency of LFX initially increases from 60.1 % to 87.2 % and then decreases to 54.4 % at a higher initial concentration. The highest degradation efficiency reaching 87.2 % can be obtained at an optimal concentration of 20 mg·L^{-1}. Likewise, the degradation efficiency of LFX also follows the pseudo first-order kinetic process (Fig. 5b) and the k_{app} values in Fig. 5c are 0.0053 min^{-1} (5 mg·L^{-1}), 0.0074 min^{-1} (10 mg·L^{-1}), 0.0086 min^{-1} (20 mg·L^{-1}), 0.0062 min^{-1} (30 mg·L^{-1}), 0.0037 min^{-1} (40 mg·L^{-1}), respectively. The inferior degradation efficiency at a lower concentration of LFX is attributed to the underutilization for the catalyst due to the insufficient contact between the catalyst and LFX. On a contrary, a higher concentration of LFX may impede the penetration of light and cover the active sites of the catalyst. Simultaneously, an increase in initial LFX concentration may generate more complex intermediates in the degradation system, finally competing with the target pollutant for ROS and consequently reducing LFX removal efficiency. Therefore, the initial concentration of LFX in subsequent experiments

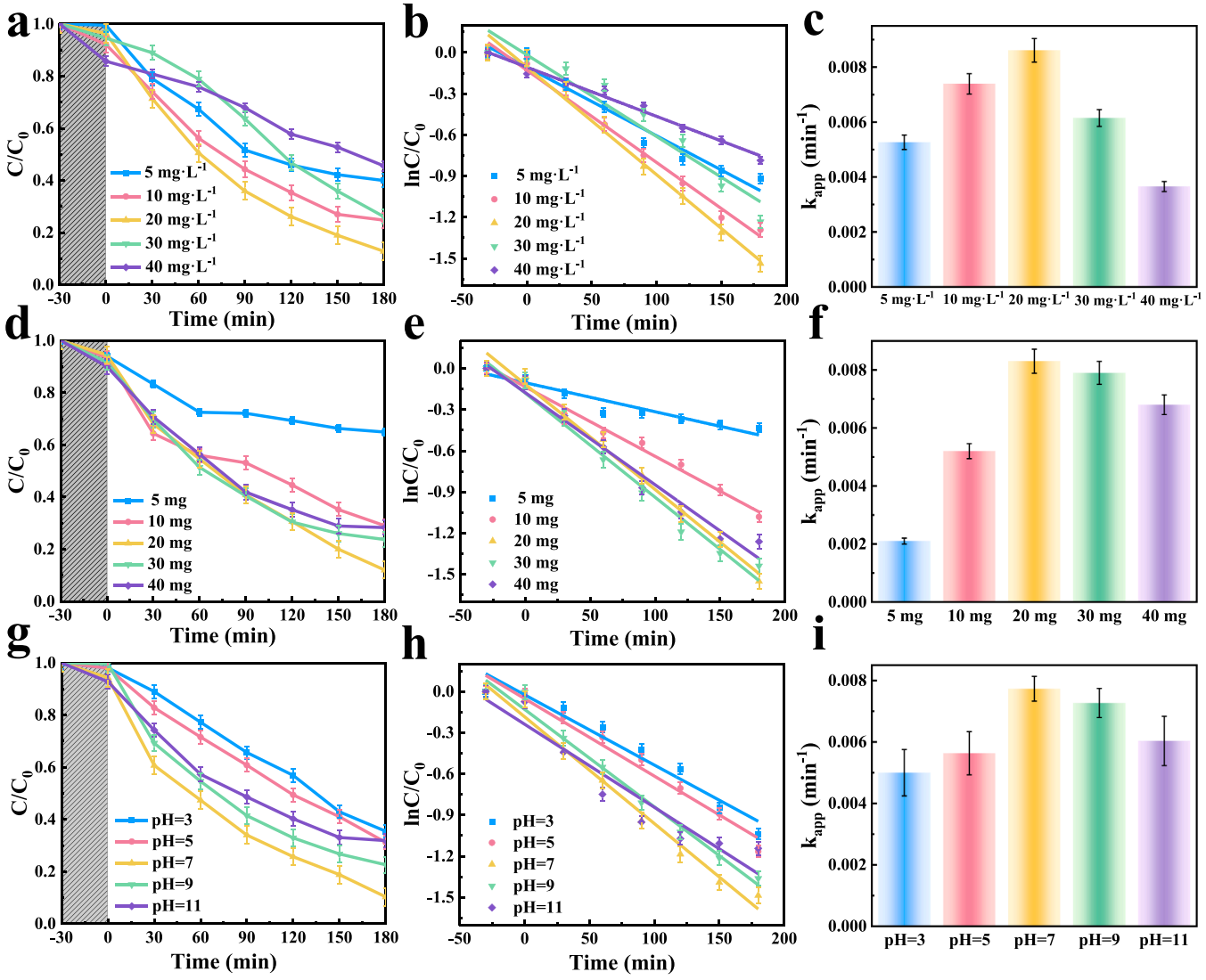

Fig. 5. Optimization of photocatalytic operation parameters for LFX by BiOBr/BiOF-PMS: (a) initial concentrations of LFX (Conditions: [catalysts] = 10 mg, pH = 7, [PMS] = 1.0 mmol·L^{-1}) (d) catalyst dosage (Condtions: [LFX] = 20 mg·L^{-1}, pH = 7, [PMS] = 1.0 mmol·L^{-1}) and (g) solution pH value (Conditions: [catalysts] = 20 mg, [LFX] = 20 mg·L^{-1}, [PMS] = 1.0 mmol·L^{-1}), (b, e, h) the profiles of the first-order kinetics derived from Fig. 5(a, d, g) and (c, f, i) the corresponding histograms of k_{app} values to Fig. 5(b, e, h). Error bars indicate the standard deviations derived from three independent experiments.

was set at 20 mg·L^{-1}.

Fig. 5d shows the effect of BiOBr/BiOF dosage on the degradation efficiency of LFX in the BiOBr/BiOF-PMS system. When the applied dosage of BiOBr/BiOF in 50 mL LFX solution increase from 5 mg to 40 mg, the photodegradation efficiencies of LFX exhibit an initial increase from 35.1 % to 88.1 % followed by a subsequent decrease to 71.7 % with further increasing the dosage and it reaches an impressive maximum degradation efficiency ~ 88.1 % at 20 mg, while the k_{app} value also achieves its highest point at 0.0083 min^{-1} (Fig. 5e, f). This change of trend can be ascribed to the increase in active sites involved in photocatalytic degradation with an increasing dosage of catalyst utilized from 5 mg to 20 mg. However, the excessive dosage of the used catalyst more than 20 mg may result in catalyst accumulation within the aqueous solution, leading to coverage of the catalytic active sites and hindering their functionality. Additionally, another possible reason is the excessive presence of the catalyst causes a shadow effect for the light within the aqueous solution, thereby diminishing light absorption efficiency.

The impact of pH on the photodegradation of LFX is shown in Fig. 5g. Similar with the above optimization on initial concentration of LFX and the catalyst dosage, the photodegradation efficiencies of LFX also shows an increase with pH value increase from 3 to 7 then gradually decrease when the pH is greater than 7. The highest photodegradation efficiency of LFX reaches 89.8 % at the optimal pH value of 7. Form Fig. 5h, we can see that the photodegradation of LFX at varied pH also obey to the pseudo first-order kinetic model. The value of k_{app} is 0.0051 min^{-1}, 0.0057 min^{-1}, 0.0078 min^{-1}, 0.0071 min^{-1} and 0.0061 min^{-1} at pH of 3, 5, 7, 9 and 11, respectively (Fig. 5i). It can be easily concluded that the neutral conditions (pH = 7) are obviously beneficial for the removal of LFX, while strong acid and strong alkali conditions can lead to the deterioration for the photodegradation toward LFX. Many aspects can be utilized to interpret this phenomenon. Firstly, in the strong acid system, the balance between protonation and deprotonation of $\bullet O_2^-$ is disrupted, finally leading to the consumption of $\bullet O_2^-$. Conversely, in extremely alkaline environments, $\bullet SO_4^-$ tends to convert into relatively low activity •OH. The strongly alkaline systems may trigger the deprotonation of PMS to weakly oxidized SO_5^{2-}, resulting in the reduction of LFX removal efficiency. However, the BiOBr/BiOF-PMS maintains stable catalytic performance within a specific range, indicating its wide adaptability to both poor acidic and basic environments. Moreover, the BiOBr/BiOF shows a zero charge point (pH_{pzc}) at approximately pH of 7.67 (**Fig. S5)**, indicating that the surface of BiOBr/BiOF exhibits positive charge at pH<7.67 and in contrast negative charge at pH>7.67. Besides, the trend in degradation efficiency is possibly attributed that the large number of H^+ in water leads to a reduction in the number of photogenerated e^- within the system at a lower pH level and on the contrary an extremely high pH value results in a significant increase in OH^- concentration which brings about a reduction of concentration of the generated h^+ and consequently causes a notable decrease in ROS such as $^1O_2$ and ·OH. Moreover, the first-order dissociation constant (pKa_1) of LFX is 5.33 and the second-order dissociation constant (pKa_2) is 8.07. When the pH of the degradation solution is below 5.33 or above 8.07, LFX carries positive and negative charges, respectively. Whereas it shows a neutral form within the pH range of 5.33 to 8.07. Therefore, BiOBr/BiOF and LFX molecules may exhibit identical charge characteristics at low and high pH levels, finally leading to mutual repulsion which is consistent with our conclusion derived from investigating the optimal pH [45]. All in all, the optimal operation conditions for LFX photodegradation by BiOBr/BiOF-PMS are 1 mmol·L^{-1} of PMS addition, 20 mg·L^{-1} of LFX, 20 mg of BiOBr/BiOF and pH = 7, ultimately leading to a significant degradation efficiency of 89.8 %. By comparison with other developed heterojunction photocatalysts based on BiOBr (**Table S2**), this developed BiOBr/BiOF heterojunction possesses relatively higher degradation performance toward LFX besides facile preparation method, proving its huge applicability in removal of antibiotic contaminants.

Besides the high photocatalytic activity, the stability and recyclability of the developed photocatalysts is another important consideration for practical applications. As illustrated in Fig. 6a, the photodegradation efficiency of LFX could still maintain above 80 % within 180 min after five runs, proving the eminent stability of BiOBr/BiOF. Meanwhile, the degree of mineralization of LFX solution was evaluated by measuring and analyzing the removal rate of TOC during the cycle experiment. As can be seen in Fig. 6a, the BiOBr/BiOF-PMS system delivers a remarkable TOC removal rate of 61.1 % for LFX at the initial cycle of the photodegradation experiment, which slightly decreases to 52.7 % after five consecutive runs, indicating that BiOBr/BiOF possesses excellent capability for mineralizing LFX into inorganic substances. Furthermore, the lower removal rate of TOC (61.1 %) compared to the photodegradation efficiency (89.8 %) during the initial run can be attributed to the formation of intermediate products. Additionally, the gradual decline of characteristic adsorption peak of LFX in the UV–vis spectra (**Fig. S6**) during the initial run indicates the eventually significant degradation of LFX and production of a series of intermediates. Generally, the degradation of LFX contaminants represents the decrease of solution toxicity. As shown in Fig. 6b and c, we can obviously observe that the diameters (1.1 cm, 1.6 cm, 1.9 cm and 2.1 cm) of the inhibitory zones of the degraded LFX solutions are significant smaller than those (1.7 cm, 2.3 cm, 2.9 cm and 3.0 cm) of the initial LFX solutions (5 mg·L^{-1}, 10 mg·L^{-1}, 20 mg·L^{-1}, 30 mg·L^{-1}), unraveling the toxicity reduction of degraded LFX solution compared to the original solution. Thereby, it can be easily concluded that the photodegradation of LFX by BiOBr/BiOF-PMS system can significantly reduce the toxicity of LFX. However, it did not reach its lowest level possibly due to incomplete mineralization within a shorter operation time. In addition, there is no significant difference for the FT-IR spectra (Fig. 6d) and SEM (Fig. 6e) of the BiOBr/BiOF before and after five runs, further implying the strong stability of BiOBr/BiOF. Furthermore, from the high resolution O1s XPS spectra of BiOBr/BiOF before and after five runs (**Fig. S7),** it can be observed that the BiOBr/BiOF after utilization shows a marginal decline for the concentration of OVs, also indicating the better stability of the BiOBr/BiOF photocatalyst. The marginal decline for the concentration of OVs could be attributed to the partial coverage on the surface of the photocatalyst by the degraded intermediates. Additionally, the stability of the BiOBr/BiOF can also be confirmed by quantificationally detecting the concentration of the dissolved Bi^{3+} from BiOBr/BiOF in the degraded solution using inductively coupled plasma mass spectrometry (ICP-MS). If all Bi^{3+} were to theoretically leach into the solution, the expected concentration would be 30.46 mg·L^{-1}. However, after the 3 h light reaction, the degradation solution exhibited a significantly lower concentration of Bi^{3+} only 49.48 μg·L^{-1}. The observed amount of leached Bi into the solution is considerably below the theoretical concentration. Hence, it can be inferred that minimal decomposition of BiOBr/BiOF occurs during the photoreaction process, indirectly confirming its eminent stability.

To further investigate the practical utilizability of the prepared BiOBr/BiOF, the photodegradation efficiencies of various contaminants including tetracycline (TC), rhodamine B (RhB), aureomycin (AM), cefalexin (CLX) and ciprofloxacin (CPFX) by BiOBr/BiOF-PMS were collected and evaluated. As shown in Fig. 6f, with an identical irradiation time of 180 min, the obtained degradation efficiencies of TC, RhB, AM, CLX and CPFX are 51.7 %, 90.2 %, 52.0 %, 34.1 % and 69.4 %, respectively, revealing that the prepared BiOBr/BiOF possesses remarkable universality toward the photocatalytic removal of a variety of refractory contaminants. The difference of the degradation efficiencies for varied target pollutants can mainly be related to the intrinsic selectivity of the synthesized photocatalyst and the complexity of the pollutants. The ROS responsible for LFX degradation by the BiOBr/BiOF-PMS system were investigated by performing the radical quenching experiments in the degradation process, in which the MeOH was used as the scavenger of •OH and $\bullet SO_4^-$ and while the IPA, p-BQ, L-his and AA were applied for trapping the •OH, $\bullet O_2^-$, $^1O_2$ and all active species, respectively. As shown in Fig. 6g, it can be seen that the introduction of AA and p-BQ into the degradation system leads to a significant decrease

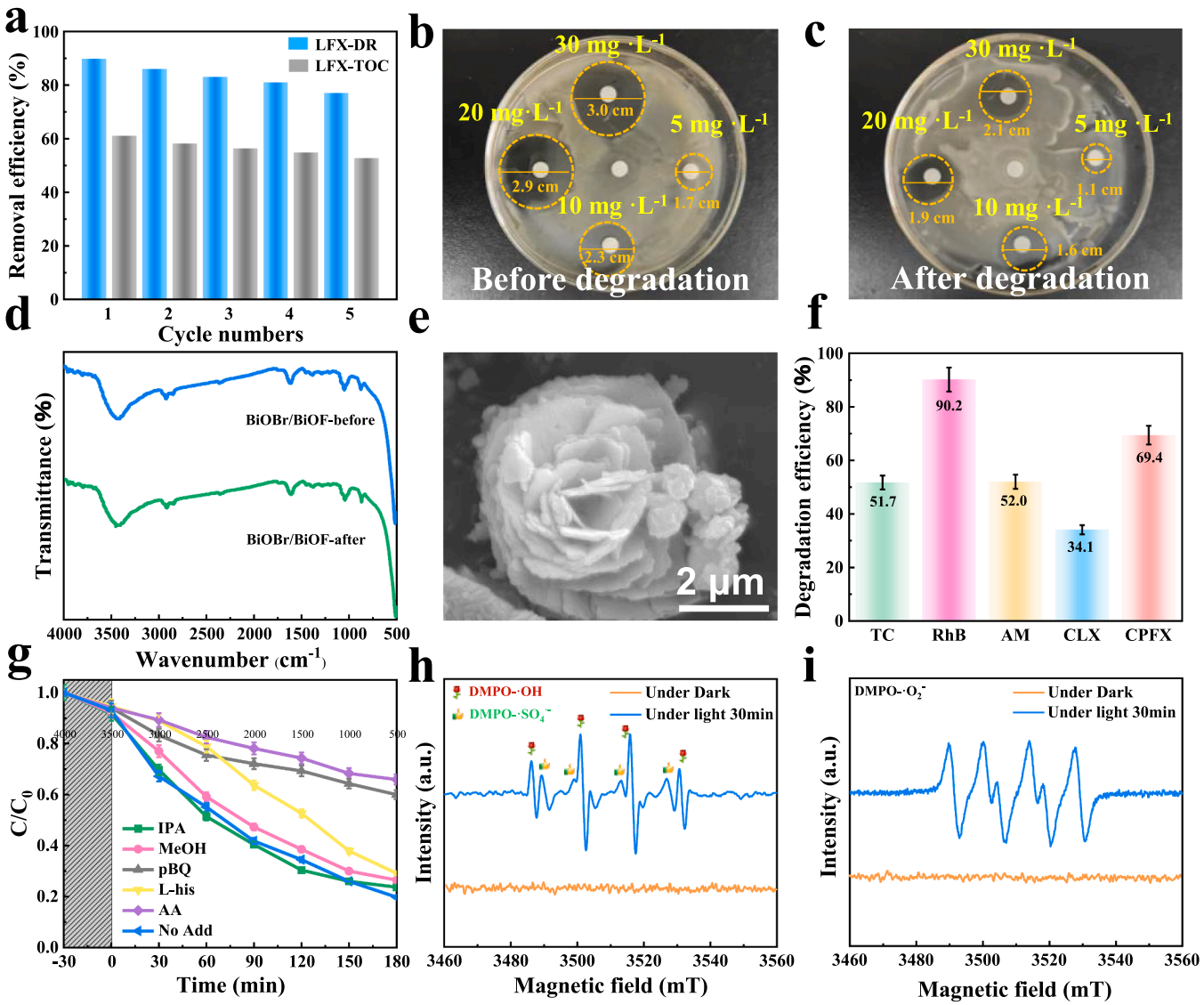

Fig. 6. (a) Cyclic photodegradation experiment and total organic carbon (TOC) removal of LFX by BiOBr/BiOF-PMS (b, c) antibacterial activity against Staphylococcus aureus of initial and degraded LFX solution (d) FT-IR spectra before and after cycling (e) SEM image of the catalyst after utilization (f) universal applicability of BiOBr/BiOF-PMS on the photodegradation toward TC, RhB, AM, CLX and CPFX. Noted that the error bars indicate the standard deviations derived from three independent experiments (g) free radicals trapping experimental results and (h, i) ESR spectra of the DMPO-•OH and $•SO_4^-$ and DMPO-$•O_2^-$ for BiOBr/BiOF-PMS system under dark and light irradiation.

in the removal rate of LFX from 89.8 % to 34.1 % and 40 %, respectively, indicating that $•O_2^-$ is the main active specie for LFX degradation. Additionally, all the other ROS including •OH, $•SO_4^-$, $^1O_2$ together with the h^+ play a subordinative role for the degradation of LFX [46,47]. ESR tests with DMPO as a spin trapping agent were performed to further verify the generated ROS in the photodegradation system. In Fig. 6h, there is no apparent ESR signal for the DMPO+ BiOBr/BiOF-PMS under dark condition, indicating there is no •OH radicals in the system. When the above systems were irradiated for 30 min, four distinctive characteristic ESR peaks of DMPO-•OH adducts with relative intensity ratio of 1:2:2:1 were observed, revealing the presence of •OH in this system [48]. Apart from the above observation, we can also discern other characteristic ESR signals of DMPO-$•SO_4^-$ adducts, confirming the generation of $•SO_4^-$ [49]. In Fig. 6i, the characteristic ESR signals with the intensity ratio 1:1:1:1 can be detected in the BiOBr/BiOF-PMS system after 30 min illumination and whereas there is no obvious ESR signal under dark condition, proving the existence of DMPO-$•O_2^-$ adducts and indirectly demonstrating the generation of $•O_2^-$ [50]. In short, the above confirmation consolidates the crucial role of •OH, $•SO_4^-$ and $•O_2^-$ responsible for the LFX degradation.

Transient photocurrent response is a widely used approach for unraveling the charge transfer and separation properties of the prepared photocatalysts. As shown in Fig. 7a, all the BiOBr, BiOF and BiOBr/BiOF exhibit regular photocurrent responses during light on/off cycle measurements under dark and visible light irradiation. Compared with the pure BiOBr and BiOF, the BiOBr/BiOF heterojunction displays the highest photocurrent intensity, suggesting its superior separation and transfer ability of the e^-/h^+. Quite obviously, heterojunction formation is the decisive factor for the improved photoelectric performance of BiOBr/BiOF, which can not only avoid excessive recombination of e^-/h^+ but also extend the lifetime of the photogenerated e^-/h^+, thus demonstrating better photocatalytic performance. Furthermore, the separation and transfer performance of the photogenerated e^-/h^+ in the photocatalysts were disclosed by measuring the photoluminescence spectra (PL). As shown in **Fig. S8**, the BiOBr/BiOF shows a lower PL emission intensity than that of BiOBr and BiOF, indicating that the photogenerated charges can be effectively separated in the BiOBr/BiOF heterojunction and the recombination of e^-/h^+ pairs can also be

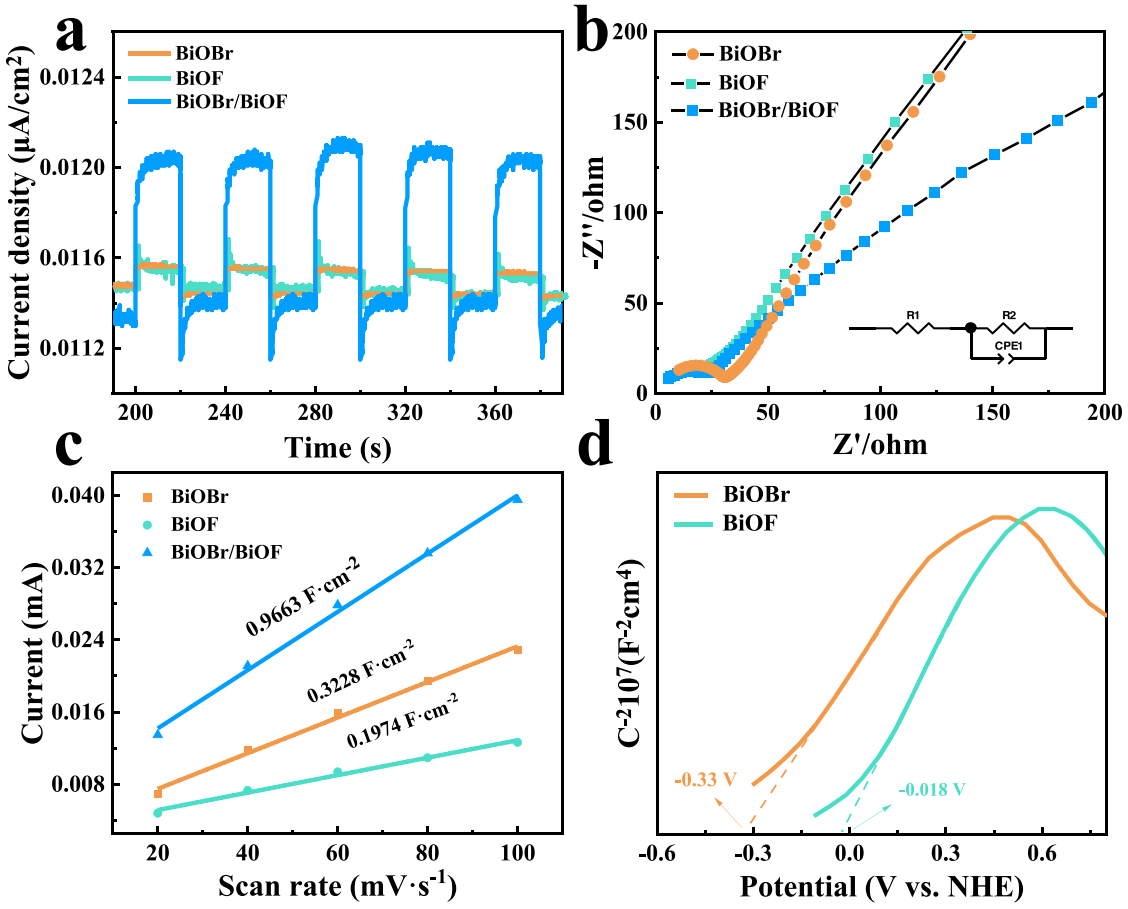

Fig. 7. (a) Transient photocurrent measurements (I-t), (b) electrochemical impedance spectra (EIS) (c) electrochemical double-layer specific capacitance (C_{DL}) tests of BiOBr, BiOF and BiOBr/BiOF and (d) Mott Schottky curves of BiOBr and BiOF, respectively.

inhibited, which is quite conducive to the photocatalytic activity. The EIS was commonly used for exploring the charges transfer resistance in the photocatalyst. From Fig. 7b and **Table S3,** we can observe that the binary BiOBr/BiOF heterojunction has smaller semi-circle in low frequency of the EIS than those of the BiOBr and BiOF monomers, revealing that the BiOBr/BiOF has smaller charges transfer resistance (R_{ct} = 1.557 Ω) than those of the BiOBr (R_{ct} = 3.537 Ω) and BiOF (R_{ct} = 3.585 Ω). Quite obviously, the smaller R_{ct} value of BiOBr/BiOF is beneficial for the rapid transfer of photogenerated e^-/h^+, finally leading to prominent photocatalytic performance. The exceptional photocatalytic performance can be closely correlated to the number of the reactive sites on the photocatalyst. By measuring the cyclic voltammetry (CV) curves of the catalysts in the non-Faraday region at different scanning rates, the C_{DL} can be obtained by fitting the relationships between current intensities of CV and scanning rates and thereby the electrochemically active surface area (ECSA) of catalysts can be estimated from the obtained C_{DL}. **Fig. S9** and Fig. 7c illustrate the CV curves and C_{DL} profiles. As shown in Fig. 7c, the sequence of C_{DL} values is BiOBr/BiOF > BiOBr > BiOF, indicating that BiOBr/BiOF had the highest surface reaction active site for photocatalytic degradation of LFX. From the Mott-Schottky plots of the BiOBr and BiOF in Fig. 7d, we can see that both of the BiOBr and BiOF display a n-type semiconductor characteristics due to the positive slopes, suggesting that their flat band edge positions (E_{fb}) correspond to their Fermi levels. By extending the Mott-Schottky curves to intersect with the horizontal axis, the E_{fb} of BiOBr and BiOF can be obtained as -0.33 eV and -0.018 eV, respectively. As commonly understand, the CB value of the n-type semiconductor is roughly equivalent to the E_{fb}. Hence, the relative positions of the CB in BiOBr and BiOF are determined to be -0.33 eV (vs. NHE) and -0.018 eV (vs. NHE), respectively [51]. Based on the equations ($E_g = E_{VB}$ - E_{CB}), the corresponding E_{VB} values of BiOBr and BiOF are 2.62 eV and 3.17 eV (vs NHE, pH = 7), respectively.

Based on the obtained energy band structures values (CB and VB) of the prepared photocatalysts, two kinds of probable photodegradation mechanisms including type II or Z-scheme can be utilized to unravel the LFX degradation mechanism by BiOBr/BiOF-PMS. As shown in Fig. 8 the BiOBr/BiOF produces carriers upon absorbing photons by the catalyst (Eq 1). In this process, the photogenerated electrons (e^-) can be excited from VB to CB in BiOBr and BiOF, while the holes (h^+) are retained in the VB of them. It is noted that the presence of defective energy levels of OVs can enhance the enrichment of the e^- and influences its transfer direction. From a thermodynamic point of view, BiOBr has a more negative E_{CB} (-0.33 eV) than that of BiOF (-0.018 eV), while BiOF has a more positive E_{VB} (3.17 eV) than that of BiOBr (2.62 eV). If the photocatalytic degradation mechanism of BiOBr/BiOF conforms to the type II illustrated in Fig. 8a, the photogenerated e^- in the CB of BiOBr will be transferred to the CB of BiOF and while the h^+ in the VB of BiOF will be transported to the VB of BiOBr. In this case, the generated e^- can react with O_2 to form $\bullet O_2^-$ and the generated h^+ would react with H_2O to produce •OH. Contrary to expectations, this pathway could not take place due to the fact of the CB potential (-0.018 eV) of the BiOF being more positive than that $O_2/\bullet O_2^-$ (-0.046 eV). This contradicts the presence of active species ($\bullet O_2^-$) identified in the results of the above free radical trapping test. Hence, it can be ventured that the Z-scheme is the suitable mechanism in the photocatalytic degradation of LFX by BiOBr/BiOF-PMS shown in Fig. 8b. After photoexcitation, the photogenerated e^- in the CB of BiOF in the Z-scheme heterojunction combines with the h^+ in the VB of BiOBr, thus retaining the h^+ with high oxidation capacity and the e^- with high reduction capacity. In addition, the activation of

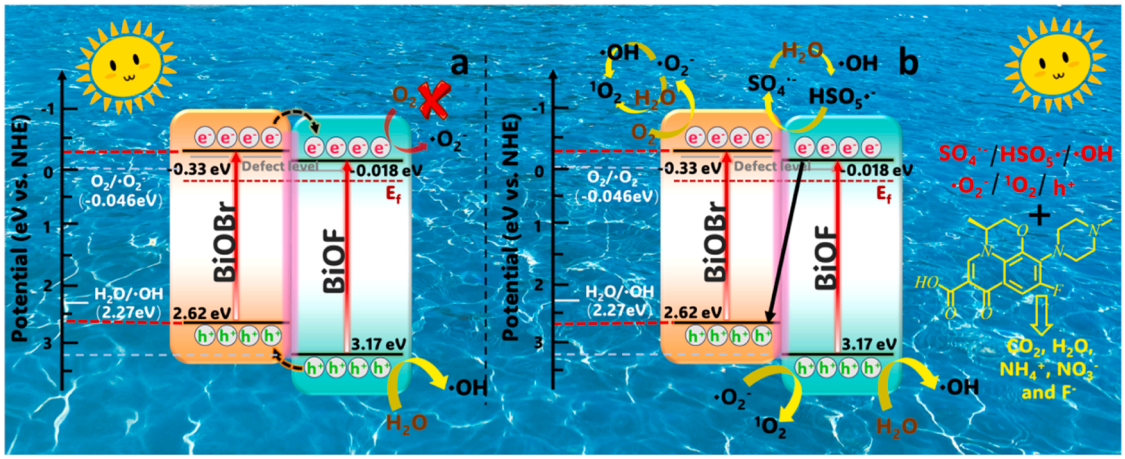

Fig. 8. The schematic illustration of the photodegradation mechanism for LFX by BiOBr/BiOF-PMS system.

PMS in the system promotes the generation of free radicals and thus enhances the photodegradation efficiency of LFX, in combination with the main ROS identified through free radical measurements ($\bullet SO_4^-$). The generated e^- and h^+ can react with O_2 and H_2O to produce $\bullet O_2^-$ and $\bullet OH$, respectively (Eq 2 and 3). The photogenerated e^- simultaneously react with PMS to form $\bullet SO_4^-$ and then the formed $\bullet SO_4^-$ converts H_2O to $\bullet OH$ (Eq 4 and 5). Subsequently, the produced $\bullet O_2^-$ in the system further react with h^+ and $\bullet OH$ to form $^1O_2$, respectively (Eq 6 and 7). Finally, LFX is converted into degradation products (CO_2, H_2O and other small molecules) through the synergistic effects of $\bullet SO_4^-$, $\bullet O_2^-$, $\bullet OH$, h^+ and $^1O_2$ by BiOBr/BiOF-PMS system (Eq 8). In conclusion, the Z-scheme mechanism in combination with the PMS activation in the BiOBr/BiOF-PMS system dominates the photodegradation of LFX and the existence of OVs can promote the enhancement of oxidation capacity.

$BiOBr/BiOF + hv \rightarrow e^- + h^+$	(1)
$e^- + O_2 \rightarrow \bullet O_2^-$	(2)
$h^+ + H_2O \rightarrow \bullet OH + H^+$	(3)
$e^- + HSO_5^- \rightarrow \bullet SO_4^- + OH^-$	(4)
$\bullet SO_4^- + H_2O \rightarrow SO_4^{2-} + \bullet OH + H^+$	(5)
$\bullet O_2^- + \bullet OH \rightarrow {}^1O_2 + OH^-$	(6)
$\bullet O_2^- + h^+ \rightarrow {}^1O_2$	(7)
$\bullet SO_4^-/ \bullet O_2^-/ \bullet OH/ h^+/ {}^1O_2 + LFX \rightarrow$ degradation products	(8)

The degradation pathways of LFX by BiOBr/BiOF-PMS system were

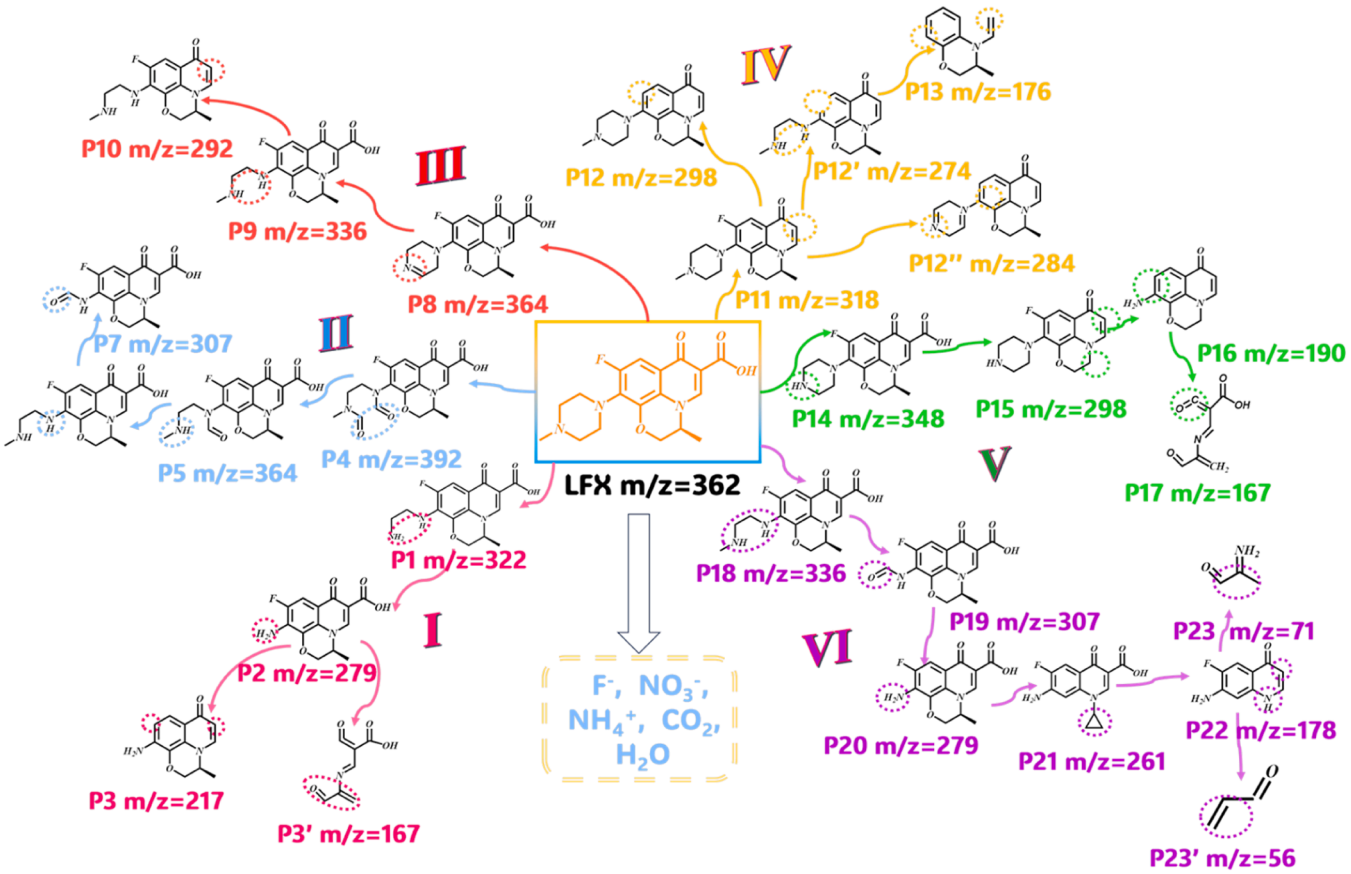

Fig. 9. Proposed photodegradation routes of LFX by BiOBr/BiOF-PMS system.

presumably inferred by analyzing the identified degradation intermediates of LFX with LC-MS technology. **Fig. S10** shows the obtained mass spectra of intermediates and **Table S4** lists their corresponding molecular structure formulas. As illustrated in Fig. 9, the degradation for LFX by BiOBr/BiOF-PMS system can be categorized into 6 types of pathways, which primarily involve three processes including carboxylation/decarboxylation, demethylation and the cleavage of piperazinyl groups attacked by the formed ROS. In pathway I, the P1 (m/z = 322) was generated due to the cleavage of the piperazine ring and following elimination of the methyl group in LFX (m/z = 362). Afterwards, P1 also underwent a structural transformation, finally resulting in the formation of P2 (m/z = 279). Subsequently, the P2 was transformed P3 (m/z = 217) or P3′ (m/z = 167) through decarboxylation and defluorination or ring-opening reaction [52]. Due to the abundant electron density in piperazine, pathway II was initiated through cleavage and oxidation of the piperazine ring, finally resulting in the generation of P4 (m/z = 392) from LFX (m/z = 362). Afterwards, the elimination of a single carbonyl group from P4 resulted in the formation of P5 (m/z = 364), while the remaining carbonyl was further eliminated to yield P6 (m/z = 336). In addition, the formation of P7 (m/z = 307) occurred through a sequence of processes involving demethylation, deamination and carbonylation of P6 [53]. The formation of P8 (m/z = 364) in pathway III is achieved through the demethylation of LFX, followed by cleavage of the N-C bond on the aromatic ring, resulting in further oxidation and the generation of P9 (m/z = 336). The degradation of the piperazine group was occurred due to ring opening caused by the attack of free radicals. Additionally, decarboxylation of P9 was occurred leading to the formation of P10 (m/z = 292) [54]. Pathway IV began with the decarboxylation process of the quinolone ring of LFX, leading to the formation of P11 (m/z = 318). The intermediate P12 (m/z = 298) was formed due to the removal of fluorine group from P11. P12′ underwent further oxidation through the breaking of the N-C bond within the aromatic ring, resulting in decarbonylation and yielding P13 (m/z = 176). Additionally, transformation of compound P11 can lead to the formation of P12″ (m/z = 284) by means of defluorination, demethylation and dehydrogenation [55]. In pathway V, the initial step of the reaction involves a direct de-methylation process that leads to the formation of P14 (m/z = 348), which subsequently underwent conversion into an amino group. Their intermediates underwent further degradation, resulting in the formation of P15 (m/z = 298) and P16 (m/z = 190) through de-carboxylation and de-piperazinylation. Furthermore, by initiating the ring opening of the benzene group, P17 (m/z = 167) was also gaine [56]. For the pathway VI, P18 (m/z = 336), P19 (m/z = 307) and P20 (m/z = 279) are initially formed by reactive radicals ($\bullet SO_4^-$ and •OH) attacking the piperazinyl group. The ring-opening of the morpholine moiety in P20 could result in the production of P21 (m/z = 261). The primary factors contributing to the generation of P22 (m/z = 178), P23 (m/z = 71) and P23′ (m/z = 56) were identified as defluorination, along with the initiation of benzene ring and quinolone ring opening processes [57]. Ultimately, LFX is fully converted into inorganic substances (such as H_2O and CO_2) through the fragmentation of functional groups and then degradation into smaller molecular components under adequate exposure to radiation over BiOBr/BiOF-PMS system.

4. Conclusion

In summary, we have developed a Z-scheme flower-like BiOBr/BiOF heterojunction photocatalyst with abundant OVs for constructing a PMS activation based AOPs (BiOBr/BiOF-PMS) technology to degrade LFX in aqueous with a facile one-step microwave-assisted hydrothermal method. After a systematical optimization on the preparation conditions of BiOBr/BiOF and the photocatalytic operation parameters by evaluating the LFX degradation, the optimal BiOBr/BiOF-PMS system delivered the highest degradation efficiency (89.8 %) toward LFX at an optimized condition of 1 mmol·L^{-1} of PMS addition, 20 mg·L^{-1} of LFX, 20 mg of BiOBr/BiOF and pH = 7, while the BiOBr and BiOF merely lead to a lower degradation efficiencies of 44.8 %and 24.0 %. This can mainly be attributed to the formation of heterojunction between BiOBr and BiOF together with the existence of abundant OVs, which can efficiently promote the separation and transfer and inhibit the recombination of the photogenerated e^-/h^+ pairs. Furthermore, the BiOBr/BiOF has better stability for multiple runs and universal applicability toward many other contaminants. The radical trapping experiments and ESR measurements confirm that the $\bullet O_2^-$ is the main active species and all the other ROS including •OH, $\bullet SO_4^-$, $^1O_2$ together with the h^+ play a subordinative role for the degradation of LFX. The degradation pathway of LFX was explored by LC-MS technique. This present study offers an efficient strategy for further improving the photocatalytic activity of the bismuth oxyhalide toward the degradation of antibiotics via PMS activation.

CRediT authorship contribution statement

Guohua Dong: Writing – original draft, Supervision, Funding acquisition, Data curation. **Dongzhe Zhang:** Writing – original draft, Methodology, Data curation. **Xinjia Zhang:** Software, Funding acquisition, Data curation. **Zhuangfang Zhang:** Validation, Methodology. **Dong-feng Chai:** Validation, Funding acquisition, Data curation. **Lijian Meng:** Validation, Software. **Wanxia Tang:** Software, Conceptualization. **Ming Zhao:** Software, Investigation. **Wenzhi Zhang:** Writing – review & editing, Supervision, Funding acquisition.

Declaration of competing interest

The authors declare that they have no known competing financial interests or personal relationships that could have appeared to influence the work reported in this paper.

The authors declare the following financial interests/personal relationships which may be considered as potential competing interests:

There are no conflicts of interest to declare. This work is original and has not been published elsewhere. We think that this manuscript is appropriate for publication in Surfaces and Interfaces.

Acknowledgments

This work was supported by the National Natural Science Foundation of China (Grant No. 32272823), the Heilongjiang Provincial Natural Science Foundation of China (Grant No. PL2024C037), the Research Foundation of Education Bureau of Heilongjiang Province of China (Grant No. 135509307) and Innovation Project of Graduate Education of Qiqihar University (Grant No. QUZLTS_CX2023032).

Supplementary materials

Supplementary material associated with this article can be found, in the online version, at doi:10.1016/j.surfin.2025.106143.

Data availability

Data will be made available on request.

References

[1] A. Dhakshinamoorthy, Z. Li, S. Yang, H. Garcia, Metal-organic framework heterojunctions for photocatalysis, Chem. Soc. Rev. 53 (2024) 3002–3035, https://doi.org/10.1039/d3cs00205e.

[2] S. Lotfi, K. Fischer, A. Schulze, A.I. Schäfer, Photocatalytic degradation of steroid hormone micropollutants by TiO_2-coated polyethersulfone membranes in a continuous flow-through process, Nat. Nanotechnol. 17 (2022) 417–423, https://doi.org/10.1038/s41565-022-01074-8.

[3] H.X. Lv, P.W. Han, X.G. Li, Z. Mu, Y. Zuo, X. Wang, Y.N. Tan, G.X. He, H.B. Jin, C. L. Sun, H.Z. Wei, L. Ma, Electrocatalytic degradation of levofloxacin, a typical antibiotic in hospital wastewater, Materials 14 (2021) 18, https://doi.org/10.3390/ma14226814.

[4] L. Peng, C. Li, X. Zhang, F. Yuan, S. Wang, J. Wang, L. Xu, Z. Sun, Persistent activation of peroxymonosulfate by MoS_2@FeOOH/ceramsite composite for

continuous flow degradation of sulfamethoxazole, J. Cent. South. Univ. 30 (2024) 3924–3939, https://doi.org/10.1007/s11771-023-5517-z.
[5] K. Stando, P. Zogornik, M. Kopiec, M. Pieszczek, K. Kowalska, E. Felis, S. Bajkacz, Degradation of fluoroquinolones and macrolides by solar light-driven heterogeneous photocatalysis - proposed drug transformation pathways, J. Photochem. Photobiol., A 453 (2024) 14, https://doi.org/10.1016/j.jphotochem.2024.115651.
[6] D. Nasuhoglu, A. Rodayan, D. Berk, V. Yargeau, Removal of the antibiotic levofloxacin (LEVO) in water by ozonation and TiO_2 photocatalysis, Chem. Eng. J. 189-190 (2012) 41–48, https://doi.org/10.1016/j.cej.2012.02.016.
[7] L. Zhang, S. Nie, T. Ai, N. Zhang, H. Wang, J. Li, J. Xu, Synthesis of amine-functionalized $CeFe_2O_4$-biochar for V(IV) and V(V) adsorption: characterization, mechanism, and regeneration capacity, Surf. Interfaces. 58 (2025) 105891, https://doi.org/10.1016/j.surfin.2025.105891.
[8] Y. Gao, D. Zou, Efficient degradation of levofloxacin by a microwave-3D $ZnCo_2O_4$/activated persulfate process: effects, degradation intermediates, and acute toxicity, Chem. Eng. J. 393 (2020) 124795, https://doi.org/10.1016/j.cej.2020.124795.
[9] N.S. Al-Bassami, La^{3+} substitution-adjusted magnetic and optical properties with enhanced photocatalytic activity and stability of copper zinc nickel ferrites for wastewater treatment applications, J. Rare Earths (2024) 03007, https://doi.org/10.1016/j.jre.2024.03.007.
[10] W. Mu, M. Gu, S. Du, Y. Chen, X. Lei, H. Chen, S. Luo, L. Wang, Extraction efficiency of metals from low-nickel matte via NH_4Cl roasting-water leaching process and synthesis of (Ni,Cu,Co)Fe_2O_4 photocatalyst, J. Cent. South. Univ. 30 (2023) 1803–1816, https://doi.org/10.1007/s11771-023-5342-4.
[11] M. Kohantorabi, G. Moussavi, S. Mohammadi, P. Oulego, S. Giannakis, Photocatalytic activation of peroxymonosulfate (PMS) by novel mesoporous Ag/ZnO@$NiFe_2O_4$ nanorods, inducing radical-mediated acetaminophen degradation under UVA irradiation, Chemosphere 277 (2021) 130271, https://doi.org/10.1016/j.chemosphere.2021.130271.
[12] Y. Luo, C. Li, Z. Liu, W. Guo, C. Sun, S. Zhao, Q. Wang, Y. Li, L. Chen, H. Zheng, F. Li, Photocatalytic activation of peroxymonosulfate (PMS) by CNN@NH_2-MIL-101(Fe) Z-scheme heterojunction for phthalates degradation under visible light irradiation, Chem. Eng. J. 481 (2024) 148683, https://doi.org/10.1016/j.cej.2024.148683.
[13] K. Zhang, Y. Zhang, D. Zhang, C. Liu, X. Zhou, H. Yang, J. Qu, D. He, Efficient photocatalytic water disinfection by a novel BP/BiOBr S-scheme heterojunction photocatalyst, Chem. Eng. J. 468 (2023) 143581, https://doi.org/10.1016/j.cej.2023.143581.
[14] H. Wu, C. Yuan, R. Chen, J. Wang, F. Dong, J. Li, Y. Sun, Mechanisms of interfacial charge transfer and photocatalytic NO oxidation on BiOBr/SnO_2 p-n heterojunctions, ACS. Appl. Mater. Interfaces. 12 (2020) 43741–43749, https://doi.org/10.1021/acsami.0c12628.
[15] Z. Xiao, X. Wu, H. Tan, S. Hao, Design and synthesis of Fe-Ce-O@C with efficient photocatalytic activity, J. Rare Earths 41 (2023) 91–99, https://doi.org/10.1016/j.jre.2022.01.007.
[16] J. Ma, L. Xu, Z. Yin, Z. Li, X. Dong, Z. Song, D. Chen, R. Hu, Q. Wang, J. Han, Z. Yang, J. Qiu, Y. Li, "One stone four birds" design atom co-sharing BiOBr/Bi_2S_3 S-scheme heterojunction photothermal synergistic enhanced full-spectrum photocatalytic activity, Appl. Catal., B 344 (2024) 123601, https://doi.org/10.1016/j.apcatb.2023.123601.
[17] J. Ma, L. Xu, Z. Yin, Z. Li, Z. Song, J. Qiu, Y. Li, Boosting charge transfer of BiOBr/AgBr S-scheme heterojunctions via interface Br atom co-sharing for enhanced visible-light photocatalytic activity, Green Energy Environ. (2024) 680257, https://doi.org/10.1016/j.gee.2024.11.003.
[18] Y. Li, J. Ma, L. Xu, T. Liu, T. Xiao, D. Chen, Z. Song, J. Qiu, Y. Zhang, Enhancement of charge separation and NIR light harvesting through construction of 2D-2D $Bi_4O_5I_2$/BiOBr:Yb^{3+}, Er^{3+} Z-scheme heterojunctions for improved full-spectrum photocatalytic performance, Adv. Sci. 10 (2023) 07514, https://doi.org/10.1002/advs.202207514.
[19] S. Lu, Y. Yin, J. Bao, H. Wang, Z. Lei, E. Hu, Q. Xin, Y. Quan, J. Li, Q. Wang, CdS@NiCr-LDH Z-scheme heterojunction with high adsorption-photocatalysis for uranium(VI) removal without any sacrificial agent, J. Environ. Chem. Eng. 12 (2024) 112989, https://doi.org/10.1016/j.jece.2024.112989.
[20] X. Dong, L. Xu, J. Ma, Y. Li, Z. Yin, D. Chen, Q. Wang, J. Han, J. Qiu, Z. Yang, Z. Song, Enhanced interfacial charge transfer and photothermal effect via in-situ construction of atom co-sharing Bi plasmonic/$Bi_4O_5Br_2$ nanosheet heterojunction towards improved full-spectrum photocatalysis, Chem. Eng. J. 459 (2023) 141557, https://doi.org/10.1016/j.cej.2023.141557.
[21] C. An, A. Sikandaier, X. Guo, Y. Zhu, H. Tang, D. Yang, Hierarchical S-scheme heterojunction of red phosphorus nanoparticles embedded flower-like CeO_2 triggering efficient photocatalytic hydrogen production, Acta Phys. 40 (2024) 2405019, https://doi.org/10.3866/pku.Whxb202405019.
[22] X. Li, Q. Dong, F. Li, Q. Zhu, Q. Tian, L. Tian, Y. Zhu, B. Pan, M. Padervand, C. Wang, Defective Bi@BiOBr/C microrods derived from Bi-MOF for efficient photocatalytic NO abatement: directional regulation of interfacial charge transfer via carbon-loading, Appl. Catal., B 340 (2024) 123238, https://doi.org/10.1016/j.apcatb.2023.123238.
[23] C.C. Dong, Z.Y. Ma, R.T. Qie, X.H. Guo, C.H. Li, R.J. Wang, Y.L. Shi, B. Dai, X. Jia, Morphology and defects regulation of carbon nitride by hydrochloric acid to boost visible light absorption and photocatalytic activity, Appl. Catal., B 217 (2017) 629–636, https://doi.org/10.1016/j.apcatb.2017.06.028.
[24] G. Huang, Z. Li, K. Liu, X. Tang, J. Huang, G. Zhang, Bismuth MOF-derived BiOBr/$Bi_{24}O_{31}Br_{10}$ heterojunctions with enhanced visible-light photocatalytic performance, Catal. Sci. Technol. 10 (2020) 4645–4654, https://doi.org/10.1039/d0cy00019a.
[25] J. Wang, C. Cao, Y. Zhang, Y. Zhang, L. Zhu, Underneath mechanisms into the super effective degradation of PFOA by BiOF nanosheets with tunable oxygen vacancies on exposed (101) facets, Appl. Catal., B (2021) 286, https://doi.org/10.1016/j.apcatb.2021.119911.
[26] G. Dong, W. Chi, D.-f. Chai, Z. Zhang, J. Li, M. Zhao, W. Zhang, J. Lv, S. Chen, A novel Ag_3BiO_3/ZnO/BC composite with abundant defects and utilizing hemp BC as charge transfer mediator for photocatalytic degradation of levofloxacin, Appl. Surf. Sci. 619 (2023) 156732, https://doi.org/10.1016/j.apsusc.2023.156732.
[27] P.M. Olmos-Moya, S. Velazquez-Martinez, C. Pineda-Arellano, J.R. Rangel-Mendez, L.F. Chazaro-Ruiz, High added value functionalized carbon quantum dots synthetized from orange peels by assisted microwave solvothermal method and their performance as photosensitizer of mesoporous TiO_2 photoelectrodes, Carbon. N. Y. 187 (2022) 216–229, https://doi.org/10.1016/j.carbon.2021.11.003.
[28] Y. Shi, J. Li, D. Huang, X. Wang, Y. Huang, C. Chen, R. Li, Specific adsorption and efficient degradation of cylindrospermopsin on oxygen-vacancy sites of BiOBr, ACS. Catal. 13 (2022) 445–458, https://doi.org/10.1021/acscatal.2c04228.
[29] M. Huang, J. Li, W. Su, X. Huang, B. Li, M. Fan, L. Dong, H. He, Oriented construction of S-doped, exposed {001} facet BiOBr nanosheets with abundant oxygen vacancies and promoted visible-light-driven photocatalytic performance, Cryst. Eng. Comm. 22 (2020) 7684–7692, https://doi.org/10.1039/d0ce01187h.
[30] Y. Guan, S. Wang, Z. Li, X. Ding, M. Wu, M. Zhang, W. Yu, Polycrystalline bismuth oxyfluoride of $BiO_{0.51}F_{1.98}$ with self-doped BiOF achieving distinctly enhanced photocatalytic activity, Mater. Lett. 262 (2020) 127197, https://doi.org/10.1016/j.matlet.2019.127197.
[31] R. Zhou, Z. Liu, S. Yao, Y. Li, Y. Fu, Harnessing oxygen vacancy-enriched and carbon-doped steric hindrance of BiOBr-OVs for superior photocatalytic pollutant degradation surf, Interfaces. 59 (2025) 105927, https://doi.org/10.1016/j.surfin.2025.105927.
[32] M. Huang, J. Xiong, X. Xiao, Z. Jiang, Y. Liang, Y. Cai, Y. Zeng, Y. Chen, $BiOIO_3$/$Bi_{12}SiO_{20}$ core-shell S-type heterojunction for efficient photocatalytic removal of bisphenol A: performance and mechanism study, J. Environ. Chem. Eng. 12 (2024) 113455, https://doi.org/10.1016/j.jece.2024.113455.
[33] G. Li, J. Yang, X. Yang, M. Liu, B. Liu, Z. Li, K. Bao, Y. Wang, Z. Wang, H. Zhou, Nitrogen-doped BiOBr nanosheets with preferentially exposed (102) facets enhanced visible-light photoreactivity, New. J. Chem. 47 (2023) 2983–2994, https://doi.org/10.1039/d2nj04676h.
[34] A. Luchen, Y. Huanshun, W. Suo, W. Jun, G. Xiaolong, Y. Xianqiang, D. Kunpeng, J. Peng, S. Huimin, One-pot preparation of Bi/BiOF/$Bi_2O_2CO_3$ Z-scheme heterojunction with enhanced photocatalysis activity for ciprofloxacin degradation under simulated sunlight, Mater. Today Nano 25 (2024) 100446, https://doi.org/10.1016/J.MTNANO.2023.100446.
[35] C. Zhou, X. Shi, D. Li, Q. Song, Y. Zhou, D. Jiang, W. Shi, Oxygen vacancy engineering of BiOBr/HNb_3O_8 Z-scheme hybrid photocatalyst for boosting photocatalytic conversion of CO_2, J. Colloid. Int. Sci. 599 (2021) 245–254, https://doi.org/10.1016/j.jcis.2021.04.064.
[36] X. Ren, J. Li, X. Cao, B. Wang, Y. Zhang, Y. Wei, Synergistic effect of internal electric field and oxygen vacancy on the photocatalytic activity of $BiOBr_xI_{1-x}$ with isomorphous fluorine substitution, J. Colloid. Int. Sci. 554 (2019) 500–511, https://doi.org/10.1016/j.jcis.2019.07.034.
[37] Z. Long, G. Zhang, H. Du, J. Zhu, J. Li, Preparation and application of BiOBr-Bi_2S_3 heterojunctions for efficient photocatalytic removal of Cr(VI), J. Hazard. Mater. 407 (2021) 124394, https://doi.org/10.1016/j.jhazmat.2020.124394.
[38] C. Wang, W. Ran, P. Du, W. Li, L. Luo, D. Wang, Enhanced visible light-driven photocatalytic activities and photoluminescence characteristics of BiOF nanoparticles determined via doping engineering, Inorg. Chem. 59 (2020) 11801–11813, https://doi.org/10.1021/acs.inorgchem.0c01811.
[39] J. Wu, X. Xi, W. Zhu, Z. Yang, P. An, Y. Wang, Y. Li, Y. Zhu, W. Yao, G. Jiang, Boosting photocatalytic hydrogen evolution via regulating Pt chemical states, Chem. Eng. J. 442 (2022) 136334, https://doi.org/10.1016/j.cej.2022.136334.
[40] M. Xu, X. Jiang, J. Li, F. Wang, K. Li, X. Cheng, Self-assembly of a 3D hollow BiOBr@Bi-MOF heterostructure with enhanced photocatalytic degradation of dyes, ACS. Appl. Mater. Int. 13 (2021) 56171–56180, https://doi.org/10.1021/acsami.1c16612.
[41] M. Yadav, S. Garg, A. Chandra, K. Hernadi, Quercetin-sensitized BiOF nanostructures: an investigation on photoinduced charge transfer and regeneration process for degradation of organic pollutants, J. Photochem. Photobiol., A 383 (2019) 112014, https://doi.org/10.1016/j.jphotochem.2019.112014.
[42] Y. Wang, K. Wang, J. Wang, X. Wu, G. Zhang, Sb_2WO_6/BiOBr 2D nanocomposite S-scheme photocatalyst for NO removal, J. Mater. Sci. Technol. 56 (2020) 236–243, https://doi.org/10.1016/j.jmst.2020.03.039.
[43] Y. Liu, J. Cui, Y. Liang, W. An, H. Wang, L. Liu, J. Hu, W. Cui, Construction of Z-scheme heterojunction of PANI-Ag-CN sandwich structure with efficient photocatalytic hydrogen evolution, Appl. Surf. Sci. 509 (2020) 145296, https://doi.org/10.1016/j.apsusc.2020.145296.
[44] K. Aktas, H. Liu, I.A. Basar, C. Eskicioglu, Adsorption enhanced biological treatment of hydrothermal liquefaction aqueous phase derived from municipal sludge, %J. Biores. Technol. 407 (2024) 131093.
[45] S.G. Fard, M. Haghighi, M. Shabani, Facile one-pot ultrasound-assisted solvothermal fabrication of ball-flowerlike nanostructured $(BiOBr)_x(Bi_7O_9I_3)_{1-x}$ solid-solution for high active photodegradation of antibiotic levofloxacin under sun-light, Appl. Catal., B 248 (2019) 320–331, https://doi.org/10.1016/j.apcatb.2019.02.021.
[46] W. Yu, J. Zhang, Y. Xiong, Z. Wan, J. Zhu, Y. Zhang, Construction of UiO-66-NH_2/BiOBr heterojunctions on carbon fiber cloth as macroscale photocatalyst for purifying antibiotics, J. Cleaner Prod. 415 (2023) 137603, https://doi.org/10.1016/j.jclepro.2023.137603.

[47] P. Gao, Z. Zhang, L. Feng, Y. Liu, Z. Du, L. Zhang, Novel Ti_3C_2/Bi@BiOI nanosheets with gradient oxygen vacancies for the enhancement of spatial charge separation and photocatalytic performance: the roles of reactive oxygen and iodine species, Chem. Eng. J. 426 (2021) 130764, https://doi.org/10.1016/j.cej.2021.130764.
[48] Y. Wan, H. Wang, J. Liu, J. Li, W. Zhou, J. Zhang, X. Liu, X. Song, H. Wang, P. Huo, Removal of polyethylene terephthalate plastics waste via Co-CeO_2 photocatalyst-activated peroxymonosulfate strategy, Chem. Eng. J. 479 (2024) 147781, https://doi.org/10.1016/j.cej.2023.147781.
[49] S. Feng, T. Xie, J. Wang, J. Yang, D. Kong, C. Liu, S. Chen, F. Yang, M. Pan, J. Yang, H. Du, H. Chen, Photocatalytic activation of PMS over magnetic heterojunction photocatalyst $SrTiO_3$/$BaFe_{12}O_{19}$ for tetracycline ultrafast degradation, Chem. Eng. J. 470 (2023) 143900, https://doi.org/10.1016/j.cej.2023.143900.
[50] X. Zhou, Y. Tian, J. Luo, B. Jin, Z. Wu, X. Ning, L. Zhan, X. Fan, T. Zhou, S. Zhang, X. Zhou, MoC quantum dots@N-doped-carbon for low-cost and efficient hydrogen evolution reaction: from electrocatalysis to photocatalysis, Adv. Funct. Mater. 32 (2022) 01518, https://doi.org/10.1002/adfm.202201518.
[51] H. Li, Q. Song, S. Wan, C.W. Tung, C. Liu, Y. Pan, G. Luo, H.M. Chen, S. Cao, J. Yu, L. Zhang, Atomic interface engineering of single-atom Pt/TiO_2-Ti_3C_2 for boosting photocatalytic CO_2 reduction, Small. 19 (2023) 01711, https://doi.org/10.1002/smll.202301711.
[52] L. Zhang, L. Tan, Z. Yuan, B. Xu, W. Chen, Y. Tang, L. Li, J. Wang, Engineering of $Bi_2O_2CO_3$/$Ti_3C_2T_x$ heterojunctions co-embedded with surface and interface oxygen vacancies for boosted photocatalytic degradation of levofloxacin, Chem. Eng. J. 452 (2023) 139327, https://doi.org/10.1016/j.cej.2022.139327.
[53] P. Han, G. Dong, X. Zhang, D. Chai, T. Su, Z. Zhang, M. Zhao, J. Li, W. Zhang, Microwave-assisted preparation of Z scheme heterojunction by anchoring $ZnFe_2O_4$ on tubular-like g-C_3N_4 for peroxymonosulfate activation towards levofloxacin degradation, J. Cent. South. Univ. (2025), https://doi.org/10.1007/s11771-025-5872-z.
[54] J. Nie, X. Yu, Z. Liu, J. Zhang, Y. Ma, Y. Chen, Q. Ji, N. Zhao, Z. Chang, Energy band reconstruction mechanism of Cl-doped Cu_2O and photocatalytic degradation pathway for levofloxacin, J. Cleaner Prod. 363 (2022) 132593, https://doi.org/10.1016/j.jclepro.2022.132593.
[55] H. Wei, F. Meng, W. Yu, J. Li, H. Zhang, Highly efficient photocatalytic degradation of levofloxacin by novel S-scheme heterojunction Co_3O_4/Bi_2MoO_6@g-C_3N_4 hollow microspheres: performance, degradation pathway and mechanism, Sep. Purif. Technol. 318 (2023) 123940, https://doi.org/10.1016/j.seppur.2023.123940.
[56] M. Arya, M. Kaur, A. Kaur, S. Singh, P. Devi, S.K. Kansal, Hydrothermal synthesis of rGO-Bi_2WO_6 heterostructure for the photocatalytic degradation of levofloxacin, Opt. Mater. 107 (2020) 110126, https://doi.org/10.1016/j.optmat.2020.110126.
[57] J. Lyu, M. Ge, Z. Hu, C. Guo, One-pot synthesis of magnetic CuO/Fe_2O_3/$CuFe_2O_4$ nanocomposite to activate persulfate for levofloxacin removal: investigation of efficiency, mechanism and degradation route, Chem. Eng. J. 389 (2020) 124456, https://doi.org/10.1016/j.cej.2020.124456.